Progressive neuroinflammation and deficits in motor function in a mouse model with an *Epg5* pathogenic variant of Vici syndrome

Bradley T. Thornton[1], Alexandra G. Hardinger[2], Laramie Pence[3], Priyanka Prem Kumar[1], Nikolas Connolly[4], Scott J. Weir[5,6], Jay L. Vivian[1,3,7,8]

[1]Division of Clinical Genetics, Department of Pediatrics, Children's Mercy Kansas City, Kansas City MO USA

[2]Bioengineering Graduate Program, University of Kansas, Lawrence KS USA

[3]Genetically Engineered Mouse Models Core, Children's Mercy Research Institute, Children's Mercy Kansas City, Kansas City MO USA

[4]Interdisciplinary Graduate Program in Biomedical Sciences, University of Kansas Medical Center, Kansas City, KS, USA

[5]Department of Pharmacology and Toxicology, and Therapeutics, University of Kansas Medical Center, Kansas City, KS, USA

[6]Institute for Advancing Medical Innovation, University of Kansas Medical Center, Kansas City, KS, USA

[7]University of Missouri-Kansas City, Kansas City MO USA

[8]Author for correspondence:

jvivian@cmh.edu

Abstract

Background: Vici syndrome (VS) is a rare pediatric genetic disorder characterized by profound developmental delay, seizures, immune deficits, cardiomyopathy, and progressive motor dysfunction, with a median survival of approximately 42 months. This devastating condition is caused by pathogenic variants in the *EPG5* gene, which encodes a key regulator of autophagy. Loss of EPG5 function leads to the accumulation of toxic intracellular material and widespread cellular dysfunction. Currently, there are no effective treatments for VS. The underlying cellular mechanisms driving the progressive neurological decline in VS remain poorly understood. Although previous studies using *Epg5* knockout models have demonstrated severe neurological phenotypes, these models have not been comprehensively characterized for molecular and cellular deficits within the central nervous system.

Methods: We report the generation and analysis of novel genetically engineered mouse models of VS, including a strain harboring a truncating mutation that recapitulates a pathogenic variant identified in a VS patient and a strain with an *Epg5* null allele. These mutant models were used to further understand the underlying molecular deficits of the nervous system.

Results: These novel *Epg5* mutant mouse models exhibited incompletely penetrant perinatal lethality and neurological deficits were detectable by six weeks of age, which worsen over time. Histological analysis revealed widespread expansion of microglia and astrocytes throughout the central nervous system (CNS). Transcriptomic profiling of CNS tissue revealed robust neuroinflammatory signatures, implicating the activation of both microglia and astrocytes. Notably, the molecular profiles of *Epg5*-deficient mice share features with disease-associated microglia observed in other models of neurological disease and injury.

Conclusions: The analysis of these novel mouse models of Vici syndrome suggest a critical role for neuroglial activation in the pathogenesis of VS. These novel in vivo models will be a valuable platform for preclinical evaluation of therapeutic strategies targeting autophagy-related neurodegeneration in congenital disorders of autophagy.

Keywords:

Vici syndrome

EPG5

Autophagy

Microglia

Astrocyte

Neurodegeneration

Congenital disorders of autophagy

Pathogenic variant

40 **Background**

41 Vici syndrome (VS; OMIM 242840; also known as EPG5-related disorder) is a rare,
42 autosomal recessive, childhood-onset multisystem disorder that primarily affects the central
43 nervous system, cardiac function, and immune response, among other organ systems (1, 2).
44 Clinical manifestations typically emerge within the first year of life and include failure to thrive,
45 global developmental delay, recurrent infections, and cardiomyopathy. Neurological features
46 include hypotonia, seizures, progressive motor decline, and structural brain abnormalities.
47 Affected children are typically nonverbal and unable to ambulate. VS follows a relatively
48 progressive course, with a median survival of approximately 42 months; however, atypical cases
49 with survival into early adulthood have been reported (unpublished observations). Mortality is
50 commonly attributed to a combination of progressive cardiomyopathy, recurrent infections, and
51 respiratory compromise due to neuromuscular decline. Neurological deterioration is a nearly
52 universal hallmark of this disease and significantly impairs quality of life. Currently, no disease-
53 modifying therapies exist, and clinical management remains largely supportive and palliative.
54 The rarity of VS, coupled with limited access to patient-derived samples and the absence of
55 well-characterized disease models, has hindered both mechanistic understanding and
56 therapeutic development.

57 A definitive diagnosis of VS is established through genetic testing, which reveals
58 pathogenic variants in the *EPG5* gene (3). *EPG5* (Ectopic P-granules protein 5) encodes a
59 critical regulator of autophagy, facilitating the fusion of autophagosomes with lysosomes(4).
60 Most pathogenic variants identified in VS are nonsense or frameshift mutations resulting in loss
61 of function, although some missense mutations have also been reported(5). Patient-derived
62 cells exhibit impaired autophagic flux, characterized by the accumulation of undegraded
63 autophagic material due to defective *EPG5*-mediated vesicle fusion (6, 7). VS is now recognized
64 as part of a broader group of rare disorders(8) termed congenital disorders of autophagy
65 (CDAs). Deficits in autophagy may drive a range of neurological disorders and other diseases

66 (9, 10), suggesting new avenues for treatment using targeted therapies that modulate
67 autophagy.
68 Previous studies using *Epg5* knockout models have demonstrated severe neurological
69 phenotypes(11); however, the molecular and cellular mechanisms underlying the progressive
70 motor deficits in VS remain poorly understood. Moreover, no existing mouse models that
71 recapitulate patient-specific *EPG5* mutations have been reported. To address this gap, we
72 generated and characterized two novel *Epg5* mutant mouse strains: one harboring a truncating
73 *W860X* pathogenic variant identified in a patient (case report in preparation) and another
74 carrying a newly developed null allele. Both models exhibit early-onset and progressive
75 neurological phenotypes, with subtle but significant differences between alleles. Whole animal
76 deficits in motor function were are evident by six weeks of age and worsen over time.
77 Transcriptomic analyses of brain tissue from these models revealed robust neuroinflammatory
78 signatures, implicating glial activation, particularly of microglia and astrocytes, in disease
79 progression. Notably, the molecular profiles observed in *Epg5*-deficient mice share features with
80 disease-associated microglia (12) identified in models of neurodegenerative disorders such as
81 Alzheimer's disease and amyotrophic lateral sclerosis, suggesting potential mechanistic
82 overlap. These findings enhance our understanding of VS pathogenesis and provide candidate
83 biomarkers for disease monitoring. Furthermore, these models establish a critical platform for
84 preclinical evaluation of therapeutic strategies targeting this devastating disorder.
85

Methods

Animal use

All animal procedures were approved by the Children's Mercy Research Institute Institutional Animal Care and Use Committee (IACUC). All housing, experimental procedures, and monitoring fully conformed to the Guide for the Care and Use of Laboratory Animals, and all euthanasia procedures conformed with the American Veterinary Medical Association's guidelines for euthanasia. The mice were generated and maintained on a C57BL/6J genetic background, and the mutant stocks were maintained as heterozygotes by backcrossing to vendor-derived animals (Jackson Laboratories, Bar Harbor ME). Homozygous mutant mice were closely monitored for animal welfare concerns related to neurological dysfunction and removed from the study via approved euthanasia methods if any effects on welfare were identified. The animals were housed in a specific pathogen-free vivarium operating as a barrier facility in single-use disposable mouse cages (Innovive, San Diego CA) with a 12-hour light/dark cycle and maintained at 22°C +/-1.0°C and 40%+/-5% humidity. Pregnant dams and preweaning pups were fed high-fat chow and water ad libitum, and postweaning aged mice were fed standard laboratory chow and water ad libitum.

Generation of mouse strains with *Epg5 W860X* and *Epg5* knockout alleles.

The design and validation of the CRISPR reagents used for in vivo genome editing were performed as described(13). To generate the *Epg5-W860X* allele, a CRISPR target site (CCCGAATCACAGCTATCTCT) was identified in exon 14 of the mouse *Epg5* locus. To generate the *Epg5*-KO allele, a CRISPR target site (CGGGCTCTCCTGCTCGCGAC) was identified at the 5' end of exon 2 of the mouse *Epg5* locus. CRISPR reagents were synthesized as crRNAs and annealed to universal tracrRNAs (Integrated DNA Technologies, Coralville IA). Prior to

112 production, the activity of the CRISPR reagents was verified via embryo electroporation of the
113 Cas9/crRNA/tracrRNA ribonucleoprotein (RNP) complex. The *Epg5*-W860X mutant mice were
114 produced as described(14) via CRISPR-mediated genome editing and homology-directed
115 repair. Single-stranded donor DNA was designed for each allele (Supplemental Table 1) and
116 generated via DNA synthesis (Integrated DNA Technologies, Coralville IA). For *Epg5*-W860X,
117 the donor DNA incorporated a single nucleotide change, resulting in a premature stop codon in
118 exon 2 flanked by 88 bp and 68 bp of *Epg5* homology for targeting via homology-directed repair.
119 The CRISPR RNP complexes were coinjected with donor DNA into C57BL/6J zygotes, which
120 were subsequently transferred to pseudopregnant females for delivery. The resulting founders
121 were confirmed for correct targeting of the donor DNA via allele-specific PCR and sequencing
122 (Supplemental Table 1). To produce the *Epg5*-KO strain, the CRISPR reagents were
123 electroporated into C57BL/6J zygotes, which were subsequently transferred to pseudopregnant
124 females for delivery. The resulting founders were analyzed for deletions generated via
125 nonhomologous end-joining via PCR, and the nature of the resulting mutations was confirmed
126 by next-generation sequencing of PCR amplicons. One founder harboring a 22-nucleotide
127 deletion in exon 2 resulting in a frameshift mutation was expanded by breeding to generate wild-
128 type C57Bl/6J mice. Germline transmission of each desired targeted allele was confirmed in F1
129 generation pups via PCR and sequencing.
130
131
132 **Behavior analysis**
133 The analysis of motor coordination, endurance, and fatigue resistance was performed via the
134 rotarod test (Panlab, Barcelona, Spain). The mice were acclimated and housed in rooms with an
135 adjusted light–dark cycle to allow for testing during the active dark phase. Test subjects were
136 given two training days with the apparatus set at 4 rpm for 1 minute for three runs each training
137 day. One week after training, the mice were tested every two weeks with the apparatus set at a

138 ramp speed from 4–40 rpm over the course of 300 seconds. The mice were tested for three
139 trials per testing day with an intertrial interval of 10–15 minutes. Failure to initiate was defined as
140 a trial in which the animal was unable to remain on the rod for one full revolution at 4 rpm at the
141 beginning of a test. The latency to fall and speed at fall data from each trial were recorded via
142 SEDACOM 2.0 software (Panlab, Barcelona, Spain). Data visualization and statistical analysis
143 were performed via Prism software (GraphPad, Boston, MA). Statistical analysis of data from
144 wild-type and mutant mice at a given timepoint was performed via an unpaired t test.
145
146
147 **Protein** analysis
148 Spinal cord tissues from 6-month-old wild-type and mutant siblings of each of the *Epg5* mutant
149 strains were dissociated in RIPA buffer (Thermo Fisher, Waltham, MA.) with a TissueRuptor
150 homogenizer (Qiagen, Hilden, Germany.). The supernatant was collected, and a protease and
151 phosphatase inhibitor cocktail (Thermo Fisher, Waltham, MA) was added. The protein
152 concentration of the supernatant was quantified via a Pierce BCA assay (Thermo Fisher,
153 Waltham, MA) per the manufacturer's protocol. Protein samples were denatured in Laemmli
154 sample buffer (Bio-Rad Laboratories, Hercules, CA), and 20 μg of protein from each sample
155 was used for western blot analysis. Antibodies against LC3 (Cell Signaling Technology, Danvers,
156 MA) and a-Tubulin (Cell Signaling Technology, Danvers, MA) and secondary antibodies (LI-COR
157 Biosciences, Lincoln, NE) were used to detect each protein. Fluorescent imaging was
158 performed on the membrane via an Odyssey CLx Imager (LI-COR Biosciences, Lincoln, NE).
159 Each band was quantified via ImageStudioLite analysis software (LI-COR Biosciences, Lincoln,
160 NE).
161
162
163 **RNA analysis**

164 Gene expression analyses were performed via purified RNA from tissues harvested from 6-
165 month-old wild-type and homozygous mutants of each of the *Epg5* strains. The tissues were
166 lysed via Qiazol/chloroform extraction, and the RNA was purified via a Qiagen RNeasy column
167 purification kit (Qiagen, Hilden, Germany) according to the manufacturer's protocols. The
168 extracted RNA was then either given to the institutional genomics core for RNA sequencing or
169 was converted into cDNA via the use of 1 µg of total RNA for quantitative PCR. The qPCRs
170 were performed using TaqMan Gene Expression Master Mix (Thermo Fisher, Waltham, MA) and
171 the indicated probes (Supplemental Table 2). The samples were analyzed via the ViiA 7 real-
172 time PCR system (Applied Biosystems, Waltham, MA) according to the manufacturer's
173 protocols. For plotting, the expression data were normalized to the data of the wild-type control
174 siblings.
175
176
177 **RNA-Seq bioinformatics analysis**
178 Transcriptomic profiling via bulk RNA sequencing was performed on RNA from the cerebellum
179 and spinal cord of homozygous W860X mice or their wild-type control siblings. RNA sequencing
180 was performed with stranded total RNA with a RiboZero Gold library preparation kit (Illumina,
181 San Diego CA) per the manufacturer's protocols. The RNA sequences were processed for gene
182 expression quantification. Standard two-group differential expression analysis of a set of RNA-
183 seq samples processed with Kallisto(15). Output files were processed with tximport(16) to
184 collapse transcript counts to gene counts via the transcript-to-gene mapping table. The mouse
185 reference genome GRCm39 was used in the analysis. To generate a volcano plot, the
186 processed average differential expression data from the RNA-seq data consisting of 13,991
187 genes in the cerebellum and 25,527 genes in the spinal cord were inputted into Prism
188 (GraphPad, Boston, MA). For comparative differential gene expression analysis between
189 tissues, genes that had a $\log_2$(fold change) of +1/-1 and a false discovery rate (adj. p value) of

190 less than 0.01 were used. Overlapping DEGs between tissues were identified via Venny
191 (https://bioinfogp.cnb.csic.es/tools/venny/index.html). The overlapping genes were then input
192 into Ingenuity Pathway Analysis (Qiagen, Hilden, Germany) for pathway analysis and to
193 g:Profiler(17) for Gene Ontology (GO) analysis. Altered pathways and associated p values were
194 visualized via Prism (GraphPad, Boston, MA).
195
196 **Histology**
197 For histology, the tissues were processed as previously described(18). In brief, 6-month-old
198 mutant or control mice were placed under anesthesia (isofluorane) for transcardial perfusion via
199 4% paraformaldehyde in PBS. CNS tissues were then removed and fixed overnight. The tissues
200 were then washed two times in 1X PBS prior to preparation for histology.
201 For immunohistochemistry, the tissues were dehydrated and embedded in paraffin. The
202 10 μm sections were rehydrated via citrate antigen retrieval buffer for use in staining to detect
203 GFAP (HRP/DAB IHC Detection Kit, Abcam, Cambridge, UK) per the manufacturer's protocol. A
204 colorimetric reaction was performed using DAB.
205 For immunofluorescence imaging, the tissues were frozen for cryosectioning as
206 described(19). In brief, 20 μm sections were cut. Direct conjugated antibodies to detect GFAP or
207 IBA-1 were used to detect astrocytes and microglia, respectively, and costained with DAPI to
208 detect nuclei. The sections were mounted with a coverslip with Fluormount G mounting media
209 (Thermo Fisher). Immunofluorescence imaging was performed on a Zeiss Axio Observer 7
210 microscope (Zeiss, Oberkochen, Germany). For quantification, images of distinct regions of the
211 spinal cord were imported into the Imaris software package (Oxford Instruments, Oxfordshire
212 UK). For each fluorophore, an absolute intensity threshold value was adjusted via the histogram
213 and standardized for each image. A new surface was created to measure the total area of the
214 image. The summed value of the combined area from each surface was divided by the total
215 area to obtain the percentage value of positivity for each image.

216 **Results**

217 To develop mouse models that recapitulate a pathogenic *EPG5* variant associated with
218 Vici syndrome, a novel mouse strain was generated via CRISPR-mediated zygotic mutagenesis
219 (ref) on an inbred C57Bl/6J genetic background (Table 1; Supplemental Table 1). One strain
220 was engineered to carry the *Epg5 W860X* mutation, which mirrors a recently identified
221 pathogenic variant in a child with severe Vici syndrome (manuscript in preparation). For
222 comparison, a knockout (*KO*) strain was also generated by introducing a 22 bp interstitial
223 deletion near the start of exon 2, resulting in a frameshift and predicted early truncation of
224 the EPG5 protein. Following generation and colony expansion, each strain was intercrossed to
225 produce homozygous mutant mice.

226 Genotypic analysis of offspring at postnatal day 14 (P14) revealed an
227 underrepresentation of homozygous mutants for both the *W860X* and *KO* alleles (Table 2). Chi-
228 square analysis indicated that this loss was due to a reduced number of surviving males ($p =$
229 0.043 for *KO*; $p = 0.035$ for *W860X*). A small number of deceased pups at P1 were found to be
230 homozygous mutants, suggesting perinatal lethality associated with these alleles.

231 Surviving homozygous mutants were monitored longitudinally postweaning. Mice
232 homozygous for either the *W860X* or *KO* mutation were generally smaller than their wild-type
233 littermates, although only *W860X* mutants consistently exhibited reduced body size throughout
234 life (Figure 1A, B; Supplemental Figure 1). All the homozygous mutants displayed marked motor
235 deficits, particularly in hindlimb coordination. Compared with age-matched controls, mutant mice
236 exhibited abnormal hindlimb posture, characterized by a splayed stance and inability to support
237 body weight (Figure 1C, D). A moderate ataxic phenotype was evident, with wobbly, halting, and
238 slow gaits (Supplemental Movie 1). Owing to progressive motor impairment, most of the mice
239 were removed from the study by 7 months of age for animal welfare reasons (Figure 1E). No
240 sex differences were observed in the severity of motor deficits.

241 To quantitatively assess motor function, rotarod testing was conducted longitudinally
242 beginning at 8 weeks of age. Compared with their control littermates, both *W860X* and *KO*
243 homozygous mutants presented significantly impaired performance (Figure 1F-I). By 12 weeks,
244 some mutants were unable to remain on the rotating cylinder, and by 14 weeks, all *W860X*
245 homozygous mutants and, by 16 weeks, all KO homozygous mutants were unable to initiate the
246 test. Both male and female mutants were equally affected. Owing to the severity of motor
247 impairment, mutants were unable to perform additional coordination tests, such as beam
248 walking. These findings of deficits in motor function were similar to previous analysis of other
249 *Epg5* mutant mouse models(11). These studies indicate early-onset and progressive deficits in
250 survival, growth, and motor function in both *Epg5* mutant strains, with modest differences in
251 severity between the two mutant alleles analyzed.
252 Tissues from each mutant strain were collected for transcript and autophagy analyses.
253 Compared with those of wild-type controls, RNA extracted from the spinal cords of *W860X*
254 homozygous mice presented significantly lower *Epg5* transcript levels (Figure 2A). Although not
255 statistically significant, a similar trend was observed in the cerebellum (Figure 2B), suggesting
256 tissue-specific transcript instability, potentially due to nonsense-mediated decay. In contrast, the
257 transcript levels in the *KO* mice were not reduced. Western blot analysis of the LC3 protein
258 (microtubule-associated protein 1 light chain 3 alpha) was used to assess autophagy (Figure
259 2C,D; Supplemental Figure 2). Analysis of LC3 via western blotting distinguishes the
260 cytoplasmic form of LC3 (LC3-I) from the autophagosome-localized LC3 (LC3-II). LC3-II is
261 subject to autophagy-mediated degradation; this the steady state levels of LC3-II allow for an
262 assessment of autophagy. The autophagosome-associated LC3-II was markedly elevated in
263 spinal cord lysates from both mutant strains compared to tissues from wildtype controls,
264 indicating that autophagic flux was impaired and autophagosome accumulation.
265 To characterize the neurological phenotype further, bulk RNA sequencing was performed
266 on cerebellar and spinal cord tissues from 6-month-old *W860X* homozygous mice and control

267 littermates. These CNS tissues were selected because of their roles in motor control. The
268 transcriptomic profiles (n=4 of each genotype, split evenly by sex) were consistent between the
269 sexes and were combined for this analysis. A substantial number of DEGs were identified, with
270 more genes upregulated than downregulated (Figure 3A, B). Notably, genes associated with
271 glial activation, including microglial markers (*Gpnmb*, *Itgax*) and the astrocytic marker *Gfap* were
272 upregulated, suggestive of a gliosis in these tissues. Several Toll-like receptor genes, key
273 components of innate immune signaling, were also upregulated. Among the downregulated
274 genes, *Myoc* (Myocilin) was nearly absent in the spinal cord of *W860X* mutants but unchanged
275 in the cerebellum. This gene is specifically expressed in the *glia limitans superficialis*, a
276 specialized astrocyte population localized to the thin surface layer throughout the CNS.
277 Previous studies have identified distinct molecular signatures associated with microglial
278 responses to neurological injury in various mouse disease models (12) and in human
279 neurodegenerative disorders (20). Among these, a disease-associated microglia (DAM)
280 signature, also referred to as the neurodegenerative microglial phenotype (MGnD), has been
281 characterized by the upregulation of genes such as *Clec7a*, *Cst7*, and *Trem2*(12).
282 Transcriptomic analysis of CNS tissues from *Epg5 W860X* homozygous mutant mice revealed
283 upregulation of many DAM-associated genes (Figure 3D), suggesting a glial response
284 reminiscent of other CNS injury models.
285 Although distinct sets of differentially expressed genes (DEGs) were identified in the
286 cerebellum and spinal cord of *Epg5 W860X* mutants, a shared gene expression signature was
287 also observed across both tissues (Figure 3C; Supplemental Table 3). Analysis of these
288 overlapping DEGs highlighted key cellular pathways affected by the *W860X* mutation in CNS
289 tissues (Figure 3E, F). Gene ontology and pathway enrichment analyses confirmed that these
290 shared DEGs were significantly associated with inflammatory and immune responses.
291 Pathways identified in this analysis include cytokine, interferon, and complement inflammatory
292 pathways. Cellular pathways identified as neutrophil degranulation and phagosome formation

293 may suggest components of a microglial activation. Although several pathways were identified
294 with pathogen response, this analysis likely does not represent an inflammatory or cellular
295 response to microbial insult, given the specific pathogen-free status of the vivarium within which
296 these animals were housed. Collectively, these transcriptomic data define a novel and complex
297 neuroinflammatory and glial activation signature in mice carrying the *Epg5 W860X* pathogenic
298 variant that is reminiscent of other neurological disease or damage models involving neuroglia.

299 To further evaluate the expression of selected DEGs, RNA was isolated from the CNS
300 tissues of 7-month-old mutant and control mice for quantitative PCR (qPCR) analysis (Figure 4).
301 Genes were selected on the basis of the transcriptomic findings, with a focus on glial markers
302 (astrocytic and microglial), inflammatory mediators, interferon response genes, and other
303 relevant targets. All DEGs identified in the *W860X* model were also dysregulated in
304 the *Epg5 KO* mice, although with varying magnitudes (Figure 4A–D; Supplemental Figure 3,4).
305 For example, *Gpnmb* and *Gfap* expression was more severely elevated in *W860X* mutants than
306 in *KO* mice, whereas other genes presented similar expression levels across both models.
307 Notably, the severity of gene expression changes varied by tissue. *Tlr7* expression, for example,
308 was more severely affected in the cerebellum of *W860X* mutants, whereas spinal cord
309 expression levels did not differ significantly between the two models. These molecular findings
310 parallel the phenotypic severity observed in vivo, with similar levels of severity between the
311 mutant alleles, with the *W860X* mutants exhibiting somewhat more pronounced deficits than *KO*
312 mice.

313 To assess the temporal progression of the gene expression deficits associated with the
314 *Epg5* mutations, the expression of a subset of glial-specific genes was evaluated in 2- and 6-
315 month-old *W860X* and *KO* mutant mice compared with wild-type controls (Figure 5;
316 Supplemental Figure 5). The selected genes included the astrocyte marker *Gfap* and the
317 microglial markers *Gpnmb* and *Itgax*. Many of these genes were already significantly
318 upregulated at 2 months of age, particularly in the spinal cord of both mutant models (Figure

319 5A–D), and their expression increased further by 6 months. In contrast, the changes in gene
320 expression in the cerebellum of the *KO* mice were relatively modest at 2 months but became
321 more pronounced with age. These results indicate that glial phenotypes in *Epg5 W860X*
322 mutants were already apparent at early adulthood stages and progress with age, which is
323 consistent with the age of observed deficits in motor function.

324 Given the strong glial signature observed via transcriptomic and qPCR analyses,
325 histological studies were performed to assess astrocyte and microglial distribution and
326 phenotype in CNS tissues from 7-month-old *Epg5 W860X* mutants and control wildtype
327 littermates. Immunohistochemistry revealed a substantial increase in GFAP-positive astrocytes
328 across all CNS regions examined, which was consistent with elevated *Gfap* transcript levels
329 (Figure 6A, B; Figure 7A–D). Immunofluorescence staining for GFAP and the microglial marker
330 IBA1 confirmed widespread astrocyte and microglial expansion in the spinal cord (Figure 6C–N)
331 and cerebellum (Figure 7E–G) in *Epg5* mutant mice. Microglia exhibited a hypertrophic, spider-
332 like morphology with extended processes (Figure 6G, arrowhead), indicative of activation. In the
333 cerebellum, increased numbers of astrocytes and microglia were observed across multiple
334 layers, including the molecular layer (ML), internal granule layer (IGL), and white matter (WM)
335 (Figure 7F, G). Despite these cellular changes, the overall cerebellar architecture remained
336 intact.

337 While glial expansion was broadly distributed, certain white matter regions presented
338 particularly dense microglia and astrocyte accumulation. In the spinal cord, microglia were
339 notably concentrated in the dorsal funiculus (Figure 6I–K), a region containing descending
340 corticospinal and ascending sensory tracts. Additionally, both astrocytes and microglia were
341 enriched along the surface of the spinal cord (Figure 6C, D, L–N). While astrocytes are normally
342 present in this region, their numbers and process extension were markedly increased in mutants
343 (Figure 6D, M). Microglia, which are typically sparse at the surface, were also significantly
344 expanded (Figure 6M). These findings demonstrate a robust and progressive glial response in

345 the CNS of *Epg5 W860X* mutant mice, which is correlated with the observed motor deficits and

346 supports a role for glial dysfunction in the pathogenesis of Vici syndrome.

347

348

349 **Discussion**

350 The complex etiology of Vici syndrome (VS) remains incompletely understood,
351 contributing to the current lack of effective therapeutic strategies. In particular, the molecular
352 and cellular basis for the neurological manifestations of VS, which are universally present in VS
353 individuals, remain poorly characterized. This study presents the first published analysis of a
354 novel mouse model harboring a pathogenic variant in *Epg5* that mirrors a mutation identified in
355 VS patients. Specifically, the *Epg5-W860X* allele recapitulates the *EPG5-W865X* nonsense
356 mutation found in a clinically severe VS patient (manuscript in preparation). Homozygous
357 *W860X* mutant mice exhibit profound motor deficits that are comparable in severity to those
358 observed in both the *Epg5* knockout (*KO*) mice analyzed in this study and the previously
359 reported *Epg5*-deficient models(11).

360 Focusing on the molecular and cellular underpinnings of neurological dysfunction, our
361 analysis revealed previously unreported CNS phenotypes in these models. Using established
362 molecular markers, we observed widespread and progressive expansion of astrocytes and
363 microglia throughout the CNS in *Epg5* mutant mice. This glial expansion increases with age and
364 correlates with the severity of motor dysfunction, with significant motor deficits and glial marker
365 upregulation evident by two months of age. Notably, a molecular signature of
366 neuroinflammation, characterized by astrocyte and microglial expansion, suggests a
367 contributory role for glial cells in VS pathogenesis and disease progression. Previous studies
368 using *Epg5* mutant mice revealed inflammatory and immune-related phenotypes (21, 22),
369 including gastrointestinal and peripheral immune dysfunction. In conjunction with these prior
370 studies, the findings in this study suggest the presence of an inflammatory phenotype across
371 multiple organ systems in *Epg5*-mutant mice, underscoring the potential for inflammation
372 potentially contributing to the multisystemic nature of the disease. Specific CNS molecular
373 markers may thus serve as indicators of disease progression and severity.

374 Comparative analysis of the mutant alleles confirmed that the *W860X* and *KO* alleles
375 presented severe loss-of-function mutations. This aligns with the clinical severity observed in
376 the patient harboring the corresponding *W865X* mutation, who succumbed to the disease at 16
377 months of age (clinical report in preparation). The reduced *Epg5* transcript levels in *W860X*
378 mutant mice suggest that the mRNA is subject to nonsense-mediated decay. Owing to the lack
379 of a high-quality antibody for mouse EPG5, protein levels associated with the mutations
380 generated in this report could not be assessed via western blot. However, unpublished data
381 from patient-derived cells indicate that the *W860X* pathogenic variant does not produce a stable
382 truncated protein, further supporting its classification as a null allele.
383 A novel and striking observation in our study was the reduced survival of male mice
384 homozygous for either the W860X or KO allele, an outcome not previously reported in other
385 *Epg5* mutant models. This discrepancy may reflect differences in experimental design, such as
386 the depth of analysis of progeny from heterozygous intercrosses or potential residual activity of
387 the allele used in earlier studies. In humans, VS is associated with early-onset hypotonia and
388 failure to thrive. The reduced perinatal survival of homozygous mutant mouse pups may mirror
389 this clinical phenotype. Further investigations are needed to elucidate the mechanisms
390 underlying the observed male-specific lethality. Interestingly, previous studies reported sex-
391 dependent differences in microglial abundance and activity during both embryonic development
392 and adulthood(23). Future analyses of *Epg5* mutant tissues at late prenatal and early postnatal
393 stages will be critical for understanding the origins of this lethality and defining the earliest
394 manifestations of glial dysregulation associated with the defective autophagy in this model.
395 One of the most striking transcriptional changes observed in the spinal cord of *Epg5*
396 mutant mice was the downregulation of *myocilin (Myoc)*, a marker of a specialized astrocyte
397 subtype known as the *glia limitans superficialis* (GLS)(24). GLS astrocytes are localized to the
398 pial surface of the brain and spinal cord and are thought to contribute to barrier function and
399 immune surveillance. *Myoc* expression is initiated postnatally in these cells, suggesting Myoc is

400 a marker for developmental maturation of GLS cells. The substantial downregulation of *Myoc* in
401 *Epg5* mutant mice implicates a requirement for autophagy, either directly or indirectly, in the
402 survival or maturation of GLS astrocytes. Interestingly, our histological analysis revealed an
403 expansion of astrocytes and microglia at the surface of the spinal cord, suggesting that reactive
404 gliosis may interfere with GLS maturation. Further studies are needed to determine whether this
405 represents a cell-autonomous defect in GLS astrocytes or a secondary effect of microglial
406 activation and inflammation. Understanding the role of GLS astrocytes in CNS homeostasis and
407 their potential involvement in VS pathogenesis could provide new insights into how autophagy
408 deficits disrupt glial development and function.

409 Astrocytes and microglia are essential for maintaining central nervous system
410 homeostasis and play increasingly recognized roles in modulating disease progression.
411 Astrocyte homeostatic functions include synaptic maintenance, neurotransmitter recycling,
412 integrity of the blood–brain barrier, and metabolic support of neurons. Microglia, the resident
413 innate immune cells of the CNS, are responsible for the phagocytosis of cellular debris,
414 apoptotic cells, and pathogens. These glial cells not only are passive support cells but are also
415 highly dynamic, responding to environmental cues and pathological states with complex
416 molecular and functional changes. In disease or injury contexts, the functional plasticity of these
417 cell types, which can adopt a range of activation states, including proinflammatory and
418 neuroprotective phenotypes, has been revealed. Importantly, these cell types can adopt
419 phenotypes that may be either neuroprotective or neurotoxic depending on the context and
420 duration of activation. Both astrocytes and microglia can secrete cytokines and chemokines
421 depending on the activation state, which influences the local microenvironment and contributes
422 to neuroinflammatory cascades. Microglia play a critical role in synaptic pruning during
423 development and in response to injury.

424 Whole-transcriptome analysis of CNS tissues from *Epg5* mutant mice revealed a
425 signature of activated microglia resembling other mouse CNS injury or disease models (12, 25).

426 This distinct transcriptional profile, known as disease-associated microglia (DAM), also referred
427 to as the neurodegenerative microglial phenotype (MGnD), has been identified in multiple
428 models of neurodegeneration or injury. This phenotype is characterized by the upregulation of
429 genes such as *Apoe*, *Trem2*, and *Cst7*, which are not typically induced in classical inflammatory
430 responses such as lipopolysaccharide (LPS) exposure. DAM microglia are thought to play
431 complex roles in disease progression, being initially protective via microglial phagocytic activity
432 by clearing debris, but there is evidence that they may contribute to disease progression if
433 chronically activated. Future studies involving single cell analysis of microglia in the *Epg5*
434 mutant mice will be needed to uncover the spectrum of the microglial phenotypes in these mice
435 and the regional differences in microglial states within the CNS, and how these may change
436 over the course of the lifespan. There is growing appreciation for the dual roles of glial cells in
437 contributing to the pathogenesis of neurological disorders. Dysregulation of glial function has
438 been implicated in a wide range of neurodegenerative diseases(26-28), including Alzheimer's
439 disease (AD), Parkinson's disease (PD), and amyotrophic lateral sclerosis (ALS). In models of
440 AD, PD, and ALS, microglial activation has been shown to be correlated with disease
441 progression. For example, *APOE* alleles associated with increased AD risk have been linked to
442 altered microglial responses(29), whereas *SOD1* mutations in ALS models have demonstrated
443 that glial dysfunction can exacerbate motor neuron degeneration(30). These findings
444 underscore the importance of glial cells not only as responders to neuronal injury but also as
445 active participants in disease mechanisms.
446 The complex neuroinflammatory signature seen in *Epg5* mutant mice suggest that glial
447 dysfunction may be a key driver of disease progression in Vici syndrome. The localized
448 accumulation of microglia in specific regions of the spinal cord in *Epg5* mutant mice, specifically
449 in white matter, may point to possible cellular mechanisms for a role of microglia in neuronal
450 function in this model. Notably, microglial localization to specific CNS regions, such as the
451 corticospinal tract in models of ALS(31), has been associated with region-specific vulnerability.

452 Whether spatial differences in glial activation in *Epg5* mutant mice or VS remains to be
453 determined. The neurological phenotypes observed in *Epg5* mutant mice likely arise from a
454 combination of neuronal and glial dysfunction driven by impaired autophagy. Future studies
455 using primary cell cultures from these mice, as well as human induced pluripotent stem cell
456 (iPSC) models derived from VS patients(32), will be essential for dissecting the cell type-specific
457 consequences associated with EPG5 loss. The development of new mouse and cellular models
458 that allow for tissue-specific manipulation of autophagy will be critical for determining the extent
459 to which glial dysfunction contributes to disease progression in VS and other congenital
460 disorders of autophagy. Ultimately these models will be critical to determine the molecular
461 mechanisms that give rise to the complex cellular deficits seen in Vici syndrome. These studies
462 will have major implications into potential therapeutic targets.
463

464 **Conclusions**

465 This study presents a detailed analysis of novel mouse models of Vici syndrome, including a
466 strain harboring a pathogenic variant in *Epg5* that mirrors a mutation identified in VS patients.
467 These mutant strains displayed an incomplete penetrant perinatal lethality, and significant motor
468 deficits of surviving mice were evident by two months of age. Our transcriptomic analysis of
469 CNS tissues revealed a complex molecular signature of neuroinflammation. Widespread and
470 progressive expansion of astrocytes and microglia was observed throughout the CNS in these
471 mutant mice, and this glial activation correlated with age and the severity of motor dysfunction.
472 The detailed analysis of these mouse models suggests a contributory role for glial cells in the
473 pathogenesis and disease progression of Vici syndrome. These studies validate the utility of
474 these mouse models for study the progression of VS, and for use in therapeutic assessment for
475 this devastating disorder, including the potential for targeting neuroglia as therapeutic strategy.
476

477 **Abbreviations**

478 EPG5: Ectopic P Granules 5

479 VS: Vici syndrome

480 AD: Alzheimer's disease

481 PD: Parkinson's disease

482 ALS: Amyotrophic lateral sclerosis

483 iPSC: induced pluripotent stem cell

484 CNS: central nervous system

485 GLS: glia limitans superficialis

486 DAM: Disease-associated microglia

487 MGnD: neurodegenerative microglia

488 **Data availability**

489 The RNA sequencing datasets supporting the conclusions of this study will be deposited in the
490 NCBI Gene Expression Omnibus. GEO accession numbers will be provided upon completion of
491 the deposit. All other data can be found within the article and its supplementary information.

492

493 **Competing interests**

494 The authors declare that they have no competing or financial interests.

495

496 **Funding**

497 This study was supported by Mercy Research Partners of Children's Mercy Kansas City, the Vici
498 Syndrome Foundation, and Vici syndrome families.

499

500 **Author contributions**

501 All the authors read and approved the final manuscript.

502 Conceptualization: JLV, SJW

503 Investigation: BTT, LP, AGH, PPK, NC, JLV

504 Data curation: BTT,LP, AGH,PPK,JLV

505 Formal analysis: LP, JLV

506 Writing – original draft: JLV

507 Writing – review and editing: BTT,LP, AGH,PPK,JLV

508 Visualization: BTT, AGH, and JLV

509 Funding acquisition: JLV

510

511 **Acknowledgments**

512 The generation of the animal models was performed by the Genetically Engineered Mouse
513 Models Core of Children's Mercy Research Institute and the Transgenic and Gene Targeting

514 Institutional Facility of the University of Kansas Medical Center as Shared Resources of the
515 University of Kansas Cancer Center (NIH P30 CA168524). We acknowledge the efforts of Jing
516 Huang and Sarah E Tague in the Histology and Integrative Imaging of the Kansas Intellectual
517 and Developmental Disabilities Resource Center at the University of Kansas Medical Center.
518 We wish to acknowledge the efforts of cores of the Children's Mercy Research Institute,
519 including RNA sequencing and analysis were performed by the Genomic Core Service Center of
520 the Children's Mercy Research Institute, and tissue preparation and sectioning were performed
521 by the Children's Mercy Pathology Core.
522

523 **Table 1.** Summary of mutant mouse strains
524

Mouse allele	*Epg5* exon	Mutation[1]	human pathogenic variant[2]	human gnomAD variant ID	human RefSNP ID
KO	2	p.R41QfsTer8 (c.122_143del)	n/a	n/a	n/a
W860X	14	p.W860X	W865X (c. 2595G>A)	SNV : 18-45925861 - C-T	rs1160786631

525
526 [1]mouse accession number: NM_001195633.2
527 [2]human accession number: NM_020964.3

Table 2. Summary of the genotypes of offspring from intercrosses of heterozygous *Epg5* mutant mice

		***Epg5* allele**					
		KO			***W860X***		
		Total	M	F	Total	M	F
genotype	expected	107	56	51	249	126	123
wt	25%	31.8%	32.1%	31.4%	30.1%	29.4%	30.9%
het	50%	55.1%	57.1%	52.9%	51.8%	55.6%	48.0%
mut	25%	13.1%	10.7%	15.7%	18.1%	15.1%	21.1%
p value		0.014	0.043	0.261	0.023	0.035	0.280
significance		*	*	NS	*	*	NS

Total: total number of mice analyzed from heterozygous intercrosses
M: number of male mice
F: number of female mice
*: $p<0.05$ according to the chi square test
NS: not significant

References

1. Byrne S, Dionisi-Vici C, Smith L, Gautel M, Jungbluth H. Vici syndrome: a review. Orphanet J Rare Dis. 2016;11:21.

2. Dafsari HS, Ebrahimi-Fakhari D, Saffari A, Deneubourg C, Fanto M, Jungbluth H. EPG5-Related Disorder. In: Adam MP, Mirzaa GM, Pagon RA, Wallace SE, Bean LJH, Gripp KW, et al., editors. GeneReviews((R)). Seattle (WA)1993.

3. Cullup T, Kho AL, Dionisi-Vici C, Brandmeier B, Smith F, Urry Z, et al. Recessive mutations in EPG5 cause Vici syndrome, a multisystem disorder with defective autophagy. Nat Genet. 2013;45(1):83-7.

4. Wang Z, Miao G, Xue X, Guo X, Yuan C, Wang Z, et al. The Vici Syndrome Protein EPG5 Is a Rab7 Effector that Determines the Fusion Specificity of Autophagosomes with Late Endosomes/Lysosomes. Mol Cell. 2016;63(5):781-95.

5. Kane MS, Vilboux T, Wolfe LA, Lee PR, Wang Y, Huddleston KC, et al. Aberrant splicing induced by the most common EPG5 mutation in an individual with Vici syndrome. Brain. 2016;139(Pt 9):e52.

6. Hori I, Otomo T, Nakashima M, Miya F, Negishi Y, Shiraishi H, et al. Defects in autophagosome-lysosome fusion underlie Vici syndrome, a neurodevelopmental disorder with multisystem involvement. Sci Rep. 2017;7(1):3552.

7. Piano Mortari E, Folgiero V, Marcellini V, Romania P, Bellacchio E, D'Alicandro V, et al. The Vici syndrome protein EPG5 regulates intracellular nucleic acid trafficking linking autophagy to innate and adaptive immunity. Autophagy. 2018;14(1):22-37.

8. Ebrahimi-Fakhari D, Saffari A, Wahlster L, Lu J, Byrne S, Hoffmann GF, et al. Congenital disorders of autophagy: an emerging novel class of inborn errors of neuro-metabolism. Brain. 2016;139(Pt 2):317-37.

9. Stamatakou E, Wrobel L, Hill SM, Puri C, Son SM, Fujimaki M, et al. Mendelian neurodegenerative disease genes involved in autophagy. Cell Discov. 2020;6:24.

10. Klionsky DJ, Petroni G, Amaravadi RK, Baehrecke EH, Ballabio A, Boya P, et al. Autophagy in major human diseases. EMBO J. 2021;40(19):e108863.

11. Zhao H, Zhao YG, Wang X, Xu L, Miao L, Feng D, et al. Mice deficient in Epg5 exhibit selective neuronal vulnerability to degeneration. J Cell Biol. 2013;200(6):731-41.

12. Barclay KM, Abduljawad N, Cheng Z, Kim MW, Zhou L, Yang J, et al. An inducible genetic tool to track and manipulate specific microglial states reveals their plasticity and roles in remyelination. Immunity. 2024;57(6):1394-412 e8.

13. Larson MA, Gibson KA, Vivian JL. In Vivo Validation of CRISPR Reagents in Preimplantation Mouse Embryos. Methods Mol Biol. 2020;2066:47-57.

14. Larson MA. Pronuclear Microinjection of One-Cell Embryos. Methods Mol Biol. 2020;2066:27-33.

15. Bray NL, Pimentel H, Melsted P, Pachter L. Erratum: Near-optimal probabilistic RNA-seq quantification. Nat Biotechnol. 2016;34(8):888.

16. Soneson C, Love MI, Robinson MD. Differential analyses for RNA-seq: transcript-level estimates improve gene-level inferences. F1000Res. 2015;4:1521.

17. Kolberg L, Raudvere U, Kuzmin I, Adler P, Vilo J, Peterson H. g:Profiler-interoperable web service for functional enrichment analysis and gene identifier mapping (2023 update). Nucleic Acids Res. 2023;51(W1):W207-W12.

18. Bhattacherjee A, Mu Y, Winter MK, Knapp JR, Eggimann LS, Gunewardena SS, et al. Neuronal cytoskeletal gene dysregulation and mechanical hypersensitivity in a rat model of Rett syndrome. Proc Natl Acad Sci U S A. 2017;114(33):E6952-E61.

19. Yang FC, Draper J, Smith PG, Vivian JL, Shapiro SM, Stanford JA. Short Term Development and Fate of MGE-Like Neural Progenitor Cells in Jaundiced and Non-Jaundiced Rat Brain. Cell Transplant. 2018;27(4):654-65.

20. Keren-Shaul H, Spinrad A, Weiner A, Matcovitch-Natan O, Dvir-Szternfeld R, Ulland TK, et al. A Unique Microglia Type Associated with Restricting Development of Alzheimer's Disease. Cell. 2017;169(7):1276-90 e17.

21. Lu Q, Yokoyama CC, Williams JW, Baldridge MT, Jin X, DesRochers B, et al. Homeostatic Control of Innate Lung Inflammation by Vici Syndrome Gene Epg5 and Additional Autophagy Genes Promotes Influenza Pathogenesis. Cell Host Microbe. 2016;19(1):102-13.

22. Lee S, Kalugotla G, Ingle H, Rodgers R, Wu C, Wang Y, et al. Intestinal antiviral signaling is controlled by autophagy gene Epg5 independent of the microbiota. Autophagy. 2022;18(5):1062-77.

23. Han J, Fan Y, Zhou K, Blomgren K, Harris RA. Uncovering sex differences of rodent microglia. J Neuroinflammation. 2021;18(1):74.

24. Hasel P, Cooper ML, Marchildon AE, Rufen-Blanchette U, Kim RD, Ma TC, et al. Defining the molecular identity and morphology of glia limitans superficialis astrocytes in vertebrates. Cell Rep. 2025;44(3):115344.

25. Hammond TR, Dufort C, Dissing-Olesen L, Giera S, Young A, Wysoker A, et al. Single-Cell RNA Sequencing of Microglia throughout the Mouse Lifespan and in the Injured Brain Reveals Complex Cell-State Changes. Immunity. 2019;50(1):253-71 e6.

26. Heppner FL, Ransohoff RM, Becher B. Immune attack: the role of inflammation in Alzheimer disease. Nat Rev Neurosci. 2015;16(6):358-72.

27. Trainor AR, MacDonald DS, Penney J. Microglia: roles and genetic risk in Parkinson's disease. Front Neurosci. 2024;18:1506358.

28. Clarke BE, Patani R. The microglial component of amyotrophic lateral sclerosis. Brain. 2020;143(12):3526-39.

29. Yin Z, Rosenzweig N, Kleemann KL, Zhang X, Brandao W, Margeta MA, et al. APOE4 impairs the microglial response in Alzheimer's disease by inducing TGFbeta-mediated checkpoints. Nat Immunol. 2023;24(11):1839-53.

30. Bond S, Saxena S, Sierra-Delgado JA. Microglia in ALS: Insights into Mechanisms and Therapeutic Potential. Cells. 2025;14(6).

31. Migliarini S, Scaricamazza S, Valle C, Ferri A, Pasqualetti M, Ferraro E. Microglia Morphological Changes in the Motor Cortex of hSOD1(G93A) Transgenic ALS Mice. Brain Sci. 2021;11(6).

32. Mitchell MW, Grandizio C, Turan N, Requesens DV. An induced pluripotent stem cell line (CIMRi001-A) from a Vici syndrome donor with a homozygous recessive c.1007A>G (p.Q336R) mutation in the EPG5 gene. Stem Cell Res. 2022;63:102833.

Figure 1. Summary of whole animal deficits in *Epg5* mutant mouse models. A,B. Weight comparison of mutant homozygous mutants with sibling control wild-type mice at 4 weeks (**A**) and 8 weeks of age (**B**). **C-E.** Compared with control mice (**C**), *W860X* homozygous mutant mice (**D**) display poorly placed hindlimbs when attempting to bear weight at 4 months of age. Hindlimb function in homozygous *W860X* mice progressively worsened by 7 months of age (**E**). **F-I.** Assessment of the motor function of *W860X* (**F, G**) and KO (**H, I**) mutant mice via the rotarod test. Compared with age-matched control siblings, homozygous mutant mice have a poor capacity to navigate the rotarod test of coordination. Mutant mice fail the test at a lower speed of rotation ('speed at fall'; **F, H**) and at a shorter time ('latency to fall'; **G, I**) on the apparatus. At 12 weeks of age, some homozygous mutant animals are unable to initiate the rotarod test, all *W860X* mice fail at 14 weeks, and all *KO* mice fail at 16 weeks. *wt*; homozygous wild-type, *KO*; homozygous mutant for the *KO* allele; *W860X*; homozygous mutant for the *W860X* allele. Analysis of data from wild-type and mutant mice at a given timepoint was performed via an unpaired t test.

****, $p<0.0001$; ***, $p<0.001$; **, $p<0.01$. *, $p<0.05$.

Figure 1

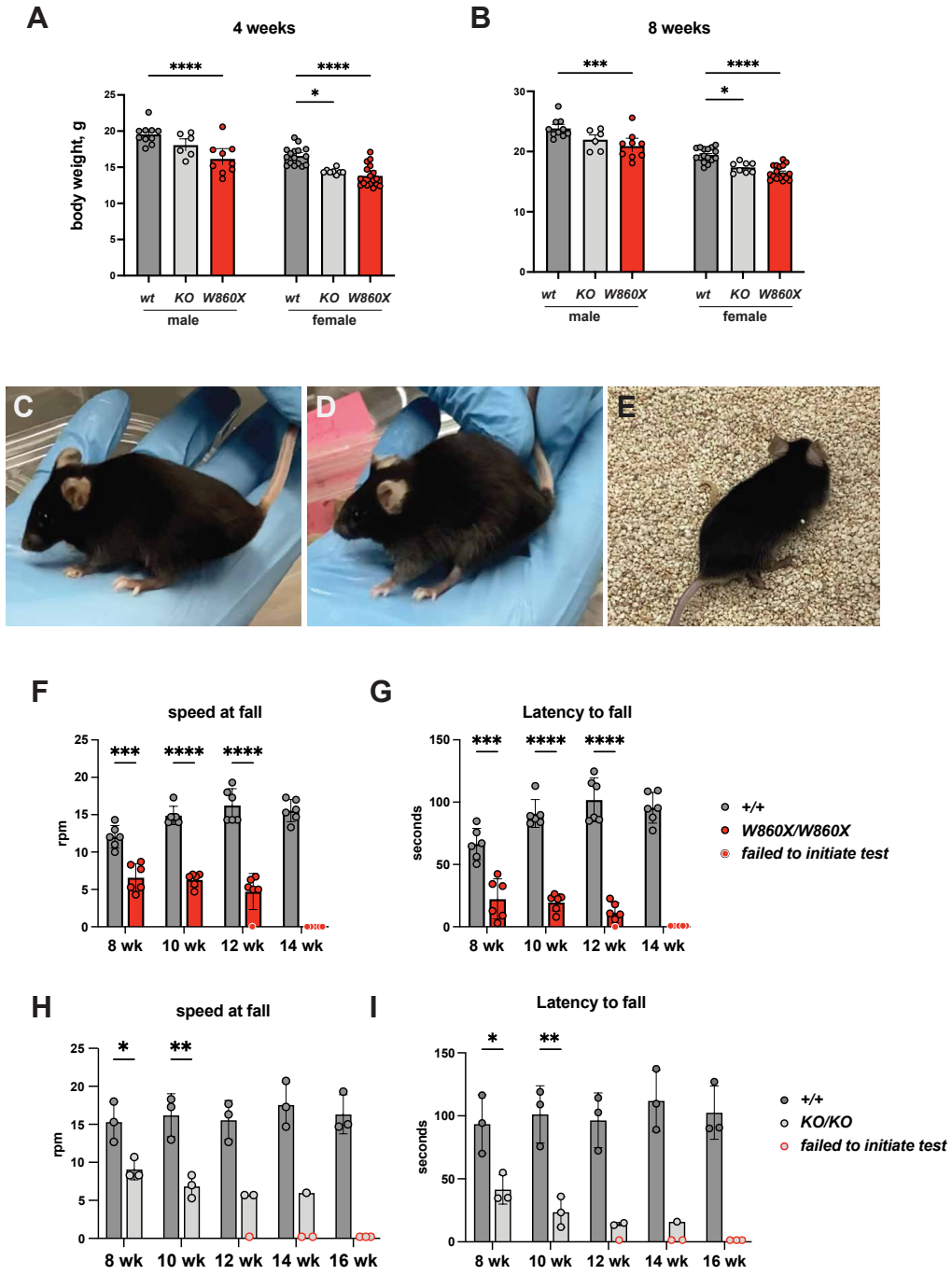
A
4 weeks
body weight, g
****
****
*
wt KO W860X
male
wt KO W860X
female
B
8 weeks
***
****
*
wt KO W860X
male
wt KO W860X
female
C
D
E
F
speed at fall
rpm
***
****
****
8 wk
10 wk
12 wk
14 wk
G
Latency to fall
seconds
***
****
****
8 wk
10 wk
12 wk
14 wk
+/+
W860X/W860X
failed to initiate test
H
speed at fall
rpm
*
**
8 wk
10 wk
12 wk
14 wk
16 wk
I
Latency to fall
seconds
*
**
8 wk
10 wk
12 wk
14 wk
16 wk
+/+
KO/KO
failed to initiate test

Figure 2. **Molecular deficits in *Epg5* transcript stability and markers of autophagy in tissues derived from *Epg5* mutant mice. A.** Assessment of *Epg5* transcript stability in control and *Epg5* mutant mice at 6 months of age via an RT–qPCR primer pair that amplifies the 3' end of the *Epg5* transcript. Unstable *Epg5* transcript in spinal cord tissue (A) from mice with mutations that recapitulate pathogenic variants. *Epg5* transcript levels in cerebellar tissues (B) were reduced but not significantly. **B,C**. Western blot analysis of the spinal cord tissue of *Epg5* mutant mice at 7 months of age was performed to detect the expression of LC3, a marker of autophagy. Note the increased accumulation of autophagosome-associated LC3-II compared with that of cytoplasmic LC3 (**C**). *wt*; homozygous wild-type, *KO*; homozygous mutant for the *KO* allele; *W860X*; homozygous mutant for the *W860X* allele. Analysis of gene expression levels between wild-type and mutant mice was performed via an unpaired t test. ***, $p<0.001$.

Figure 2

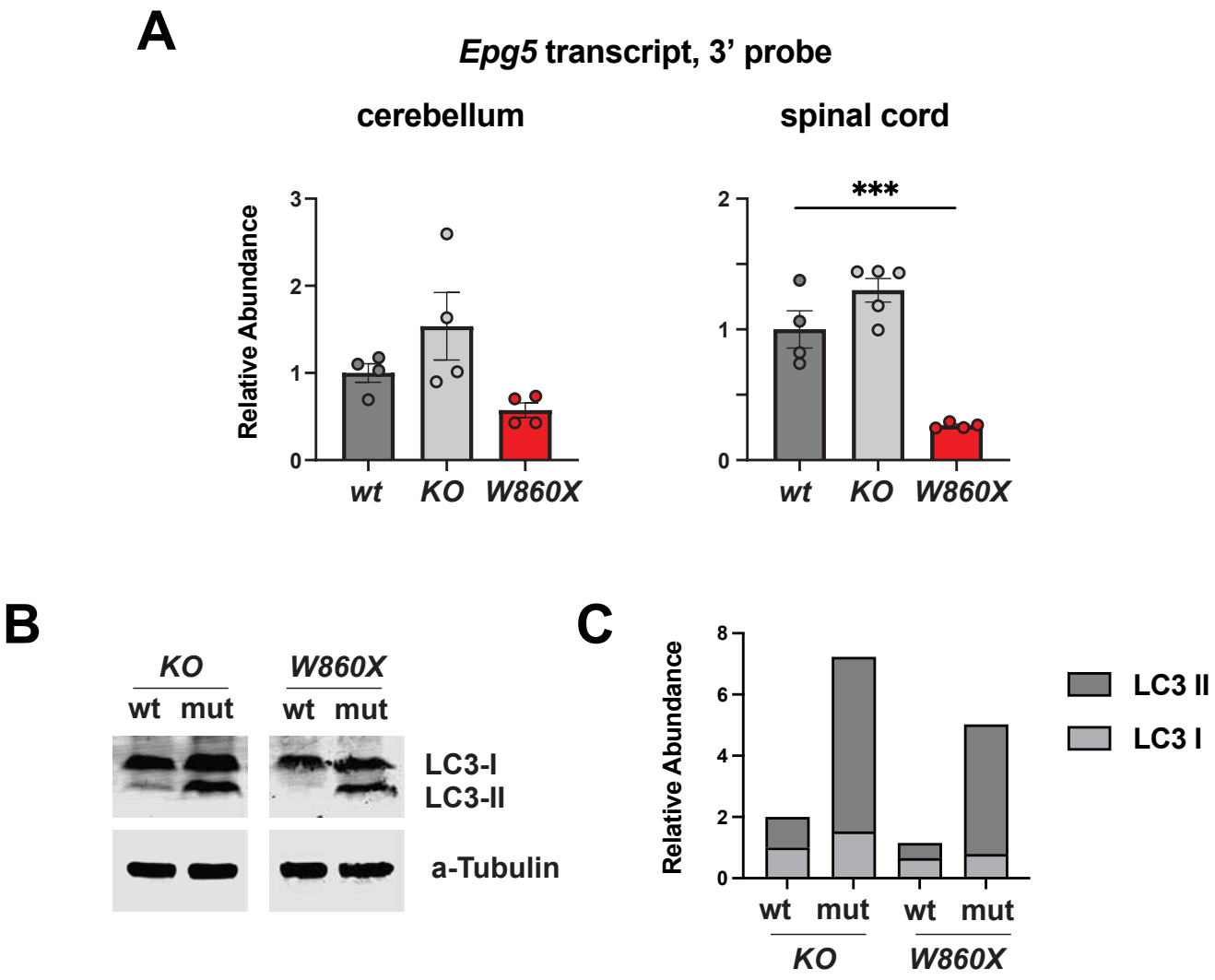
A
Epg5 transcript, 3' probe
cerebellum
spinal cord
Relative Abundance
***
wt
KO
W860X
B
KO
W860X
wt
mut
LC3-I
LC3-II
a-Tubulin
C
Relative Abundance
LC3 II
LC3 I

Figure 3. Transcriptomic analysis of CNS tissues revealed a range of molecular deficits associated with *Epg5* pathogenic variants. A,B. Volcano plot from whole-tissue transcriptomic analysis of the anterior spinal cord (**A**) and cerebellum (**B**) showing differentially expressed genes (DEGs) *in Epg5 W860X* homozygous mutant mice compared with control age-matched siblings. Select genes of interest are marked. **C.** Venn diagram of overlapping differentially expressed genes in *Epg5 W860X* mutant CNS tissues. For this analysis, genes with both 2-fold or greater up- or downregulation and adjusted P values less than 0.01 **D were identified.** Heatmap of genes differentially expressed from the spinal cord and cerebellum of *Epg5 W860X* from transcriptomic analysis of select genes associated with a previously identified disease-associated microglial signature in other mouse neurological damage models. Genes that were absent from the transcriptomic analysis of the cerebellum (*Clec7a* and *Ccl4*) were assessed via Taqman qPCR. Notably, a substantial number of these genes are upregulated in the CNS of *Epg5 W860X* mutant mice **E, F.** Gene Ontology (GO; E) and pathway analyses of the overlapping CNS DEG signature in *Epg5 W860X* mutant mice.

Figure 3

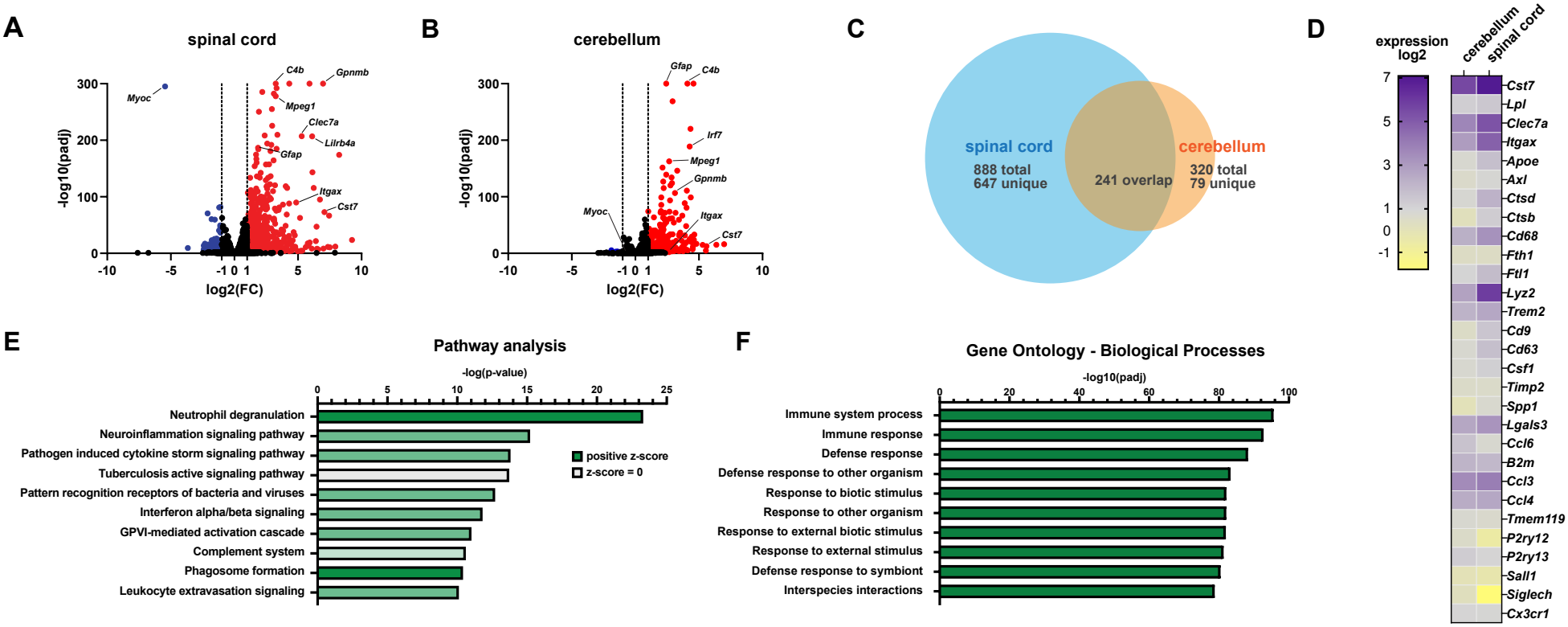
A
spinal cord
-log10(padj)
log2(FC)
Myoc
C4b
Gpnmb
Mpeg1
Clec7a
Lilrb4a
Gfap
Itgax
Cst7
B
cerebellum
Gfap
C4b
Irf7
Mpeg1
Gpnmb
Myoc
Itgax
Cst7
C
spinal cord
888 total
647 unique
241 overlap
cerebellum
320 total
79 unique
D
expression
log2
cerebellum
spinal cord
Cst7
Lpl
Clec7a
Itgax
Apoe
Axl
Ctsd
Ctsb
Cd68
Fth1
Ftl1
Lyz2
Trem2
Cd9
Cd63
Csf1
Timp2
Spp1
Lgals3
Ccl6
B2m
Ccl3
Ccl4
Tmem119
P2ry12
P2ry13
Sall1
Siglech
Cx3cr1
E
Pathway analysis
-log(p-value)
Neutrophil degranulation
Neuroinflammation signaling pathway
Pathogen induced cytokine storm signaling pathway
Tuberculosis active signaling pathway
Pattern recognition receptors of bacteria and viruses
Interferon alpha/beta signaling
GPVI-mediated activation cascade
Complement system
Phagosome formation
Leukocyte extravasation signaling
positive z-score
z-score = 0
F
Gene Ontology - Biological Processes
-log10(padj)
Immune system process
Immune response
Defense response
Defense response to other organism
Response to biotic stimulus
Response to other organism
Response to external biotic stimulus
Response to external stimulus
Defense response to symbiont
Interspecies interactions

Figure 4. Comparison of gene expression defects between *Epg5* mutant alleles. The expression of select differentially expressed genes identified from the transcriptomic analysis of *Epg5* mutant mice was examined via qPCR via TaqMan assays. **A-D**. Comparison of gene expression deficits in the spinal cord (A, B) and cerebellum (C, D) of the three *Epg5* homozygous mutant mice and age-matched sibling wild-type control mice at 6 months of age. Compared with the wild-type controls, all the mutants presented significant deficits in gene expression of these selected markers at 6 months of age. *wt*; homozygous wild-type, *KO*; homozygous mutant for the *KO* allele; *W860X*; homozygous mutant for the *W860X* allele. Analysis of gene expression levels between wild-type and mutant mice via one-way ANOVA. ****, $p<0.0001$; ***, $p<0.001$; **, $p<0.01$; *, $p<0.05$.

Figure 4

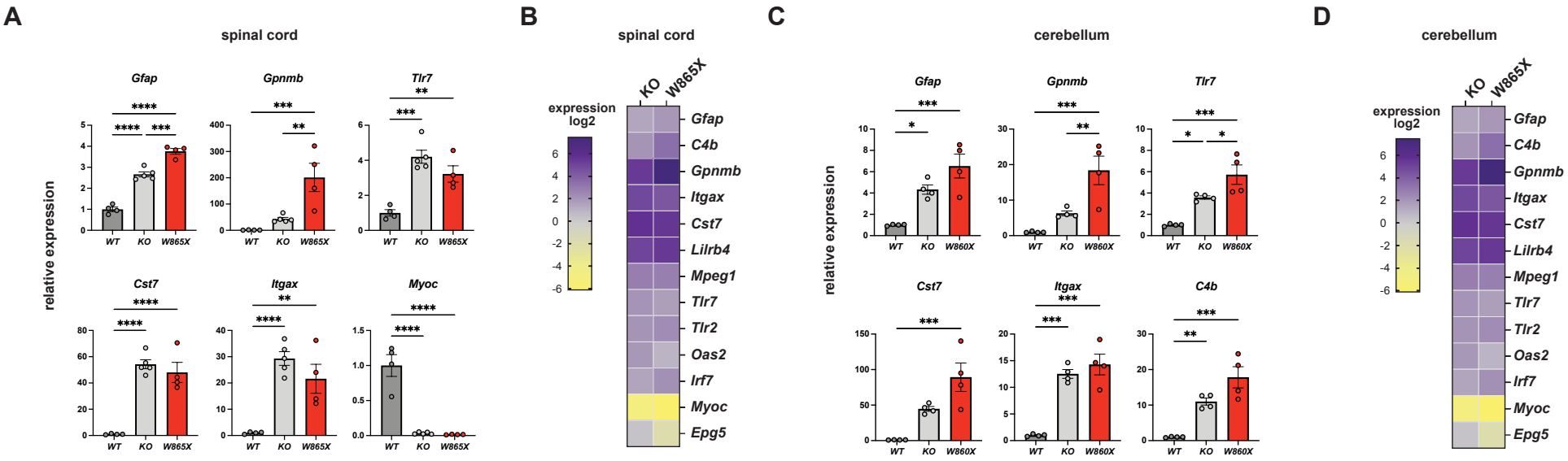
A
spinal cord
relative expression
Gfap
Gpnmb
Tlr7
Cst7
Itgax
Myoc
WT
KO
W865X
B
spinal cord
expression log2
KO
W865X
Gfap
C4b
Gpnmb
Itgax
Cst7
Lilrb4
Mpeg1
Tlr7
Tlr2
Oas2
Irf7
Myoc
Epg5
C
cerebellum
relative expression
Gfap
Gpnmb
Tlr7
Cst7
Itgax
C4b
WT
KO
W860X
D
cerebellum
expression log2
KO
W865X
Gfap
C4b
Gpnmb
Itgax
Cst7
Lilrb4
Mpeg1
Tlr7
Tlr2
Oas2
Irf7
Myoc
Epg5

Figure 5. Comparison of gene expression defects between *Epg5* mutant alleles and effects on age. Age effects on gene expression deficits in *Epg5 W860X* (**A, B**) and *Epg5 KO* (**C, D**) CNS tissues. Tissues from the anterior spinal cord (**A, C**) and cerebellum (**B, D**) were isolated from the indicated mutants between 2 months and 6 months of age for gene expression analysis. Relative expression is based on comparisons with wild-type mice at the 2-month timepoint. *wt*; homozygous wild-type, *KO*; homozygous mutant for the *KO* allele; *W860X*; homozygous mutant for the *W860X* allele. Analysis of gene expression levels between wild-type and mutant mice in a given cohort via one-way ANOVA. ****, $p<0.0001$; ***, $p<0.001$; **, $p<0.01$; *, $p<0.05$.

Figure 5

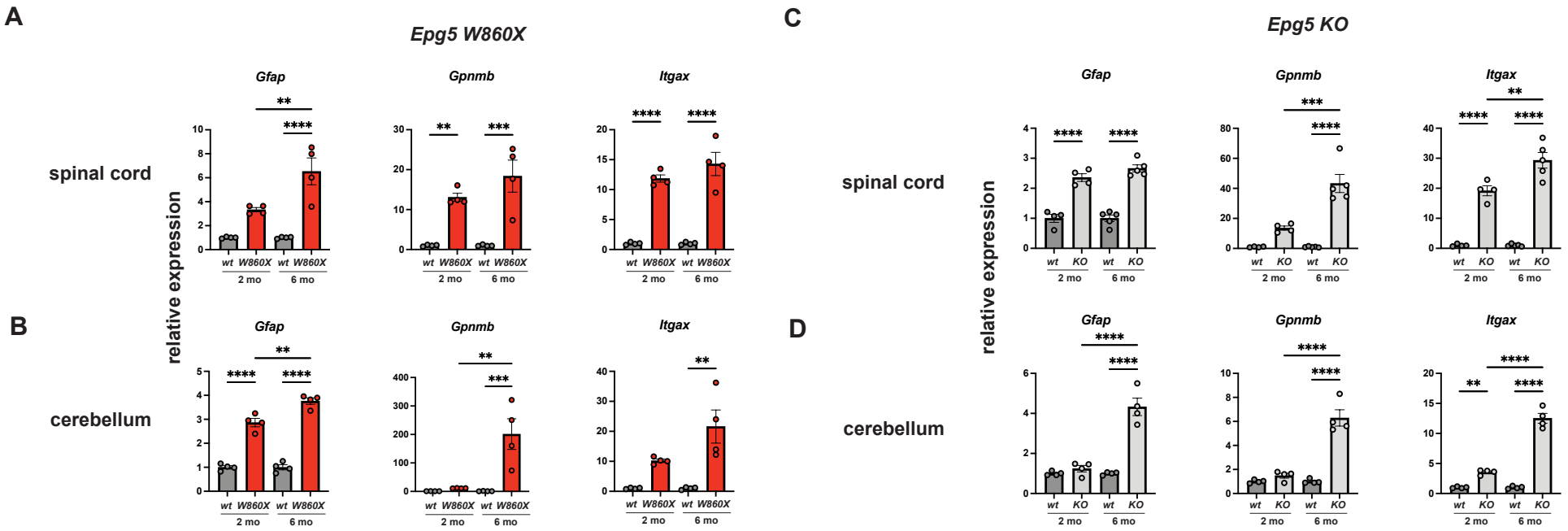
A
Epg5 W860X
Gfap
Gpnmb
Itgax
spinal cord
relative expression
wt W860X wt W860X
2 mo 6 mo
B
cerebellum
C
Epg5 KO
wt KO wt KO
D

Figure 6. Glial expansion in the spinal cord of *Epg5* mutant mice. Anterior spinal cord tissues, corresponding to the region around cervical vertebra 6 C6, were collected from 7-month-old control (**A, C, F, I, L**) or *Epg5 W860X* homozygous mutant mice (**B, D, G, J, M**) for histological analysis. **A-B.** Histochemical analysis to detect GFAP in the ventral spinal cord. A substantial increase in GFAP-positive cells was observed throughout the spinal cord in the *Epg5 W860X* homozygous mutant mice. Scale bar, 100 μm. **C–N**. Immunofluorescence was used to detect astrocytes (GFAP; green), microglia (IBA-1; red), and nuclei (DAPI; blue) in the spinal cord. **C,D.** Expanded microglia and astrocytes were observed throughout the spinal cord in the *Epg5 W860X* homozygous mutant mice. Scale bar, 300 μm. **E–N**. High-magnification assessment of microglia and astrocytes in specific regions of the spinal cord (**E**; diagram generated with Biorender). **F,G.** High-magnification image of the ventral gray matter of the spinal cord showing expanded astrocytes and microglia, with microglia demonstrating morphological changes, including thickened and more extensive processes and a large size, suggesting an activated phenotype (arrowheads). Scale bar, 100 μm. **H.** Quantification of the increase in microglia in the ventral horn gray matter of the spinal cord as a percentage of the total image area, demonstrating a quantitative increase in microglial content. **I,J.** Region of the dorsal funiculus of the spinal cord. Scale bar, 150 μm. **K.** Substantial expansion of microglia in the dorsalmost region of the dorsal funiculus. **L,M.** Details of the ventral border of the spinal cord. The top region of each image shows microglia, which are substantially increased in this region. The bottom portion of each image shows astrocytes, including the *glia limitans superficialis*, which are substantially expanded in the border region of the spinal cord. Scale bar, 100 μm. **N.** Quantification of astrocyte content in the ventral spinal cord and ventral border. Analysis of cell quantification between wild-type and mutant mice was performed via an unpaired t test. ****, $p<0.0001$.

Figure 6

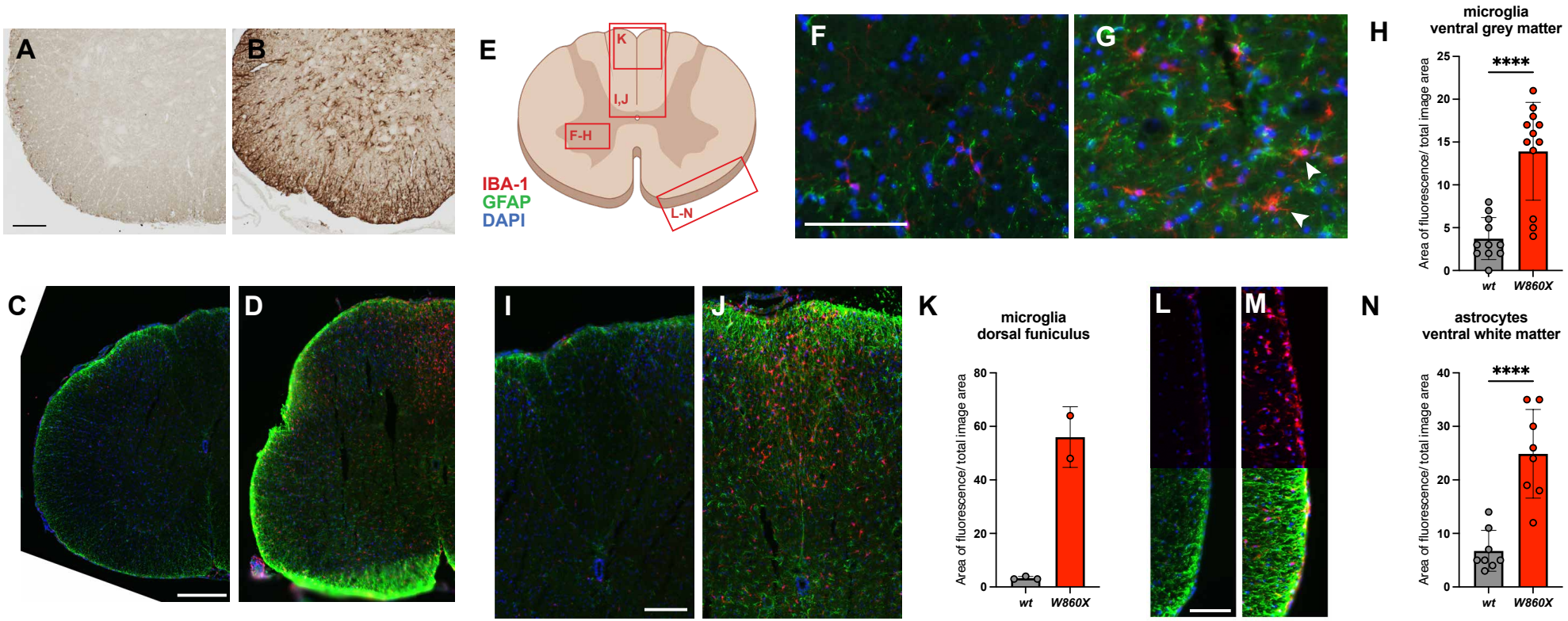
A
B
E
K
I,J
F-H
L-N
IBA-1
GFAP
DAPI
F
G
H
microglia
ventral grey matter
****
Area of fluorescence/ total image area
wt
W860X
C
D
I
J
K
microglia
dorsal funiculus
Area of fluorescence/ total image area
wt
W860X
L
M
N
astrocytes
ventral white matter
****
Area of fluorescence/ total image area
wt
W860X

Figure 7. Glial expansion in the brain and cerebellum of *Epg5* mutant mice. Whole brains were collected from 7-month-old *Epg5W860X* homozygous mutant mice for histological analysis. **A-D.** Histochemical analysis to detect GFAP, a marker of astrocytes in the brain (**A, B;** scale bar, 1 mm), and focus on the cerebellum (**C, D**) in control (**A, C**) or *Epg5 W860X* homozygous mutant mice (**B, D**). A substantial increase in GFAP-positive cells was observed throughout all regions of the brain, including the cerebellum. **E-G**. Immunofluorescence was used to detect astrocytes (GFAP; green), microglia (IBA-1; red), and nuclei (DAPI; blue) in the indicated regions of the cerebellum (E; diagram generated with Biorender) in control (**F**) or *Epg5 W860X* homozygous mutant mice (**G**). Expanded microglia and astrocytes are observed in all layers of the cerebellum of *Epg5W860X* homozygous mutant mice. Scale bar, 200 μm. Layers of the cerebellum are indicated. ML, molecular layer; PCL, Purkinje cell layer; IGL, internal granule layer; WM, white matter.

Figure 7

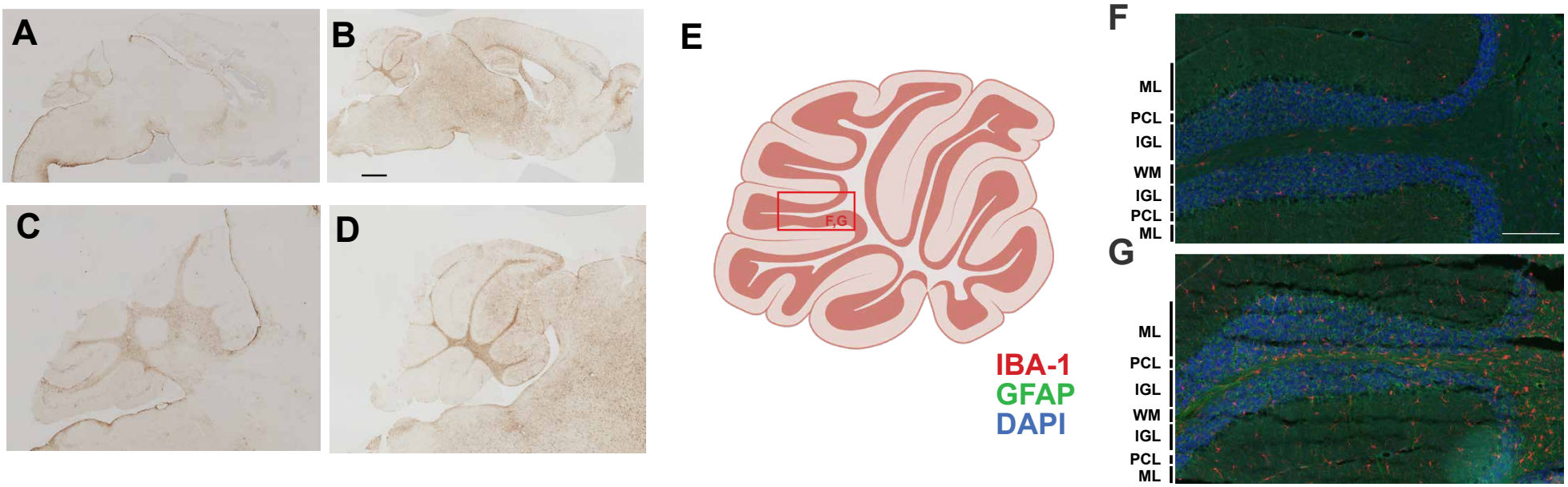
A
B
C
D
E
F,G
IBA-1
GFAP
DAPI
F
ML
PCL
IGL
WM
IGL
PCL
ML
G
ML
PCL
IGL
WM
IGL
PCL
ML

Supplemental Figure 1. Longitudinal weight data of *Epg5* mutant mice. Mice were weighed weekly to monitor weight and for monitoring animal welfare. **A, B.** Weight data for control wildtype littermates or homozygous mutant *W860X* males (**A**) or females (**B**). **C,D.** Weight data for control wildtype littermates or homozygous mutant *KO* males (**C**) or females (**D**).

Supplemental Figure 1

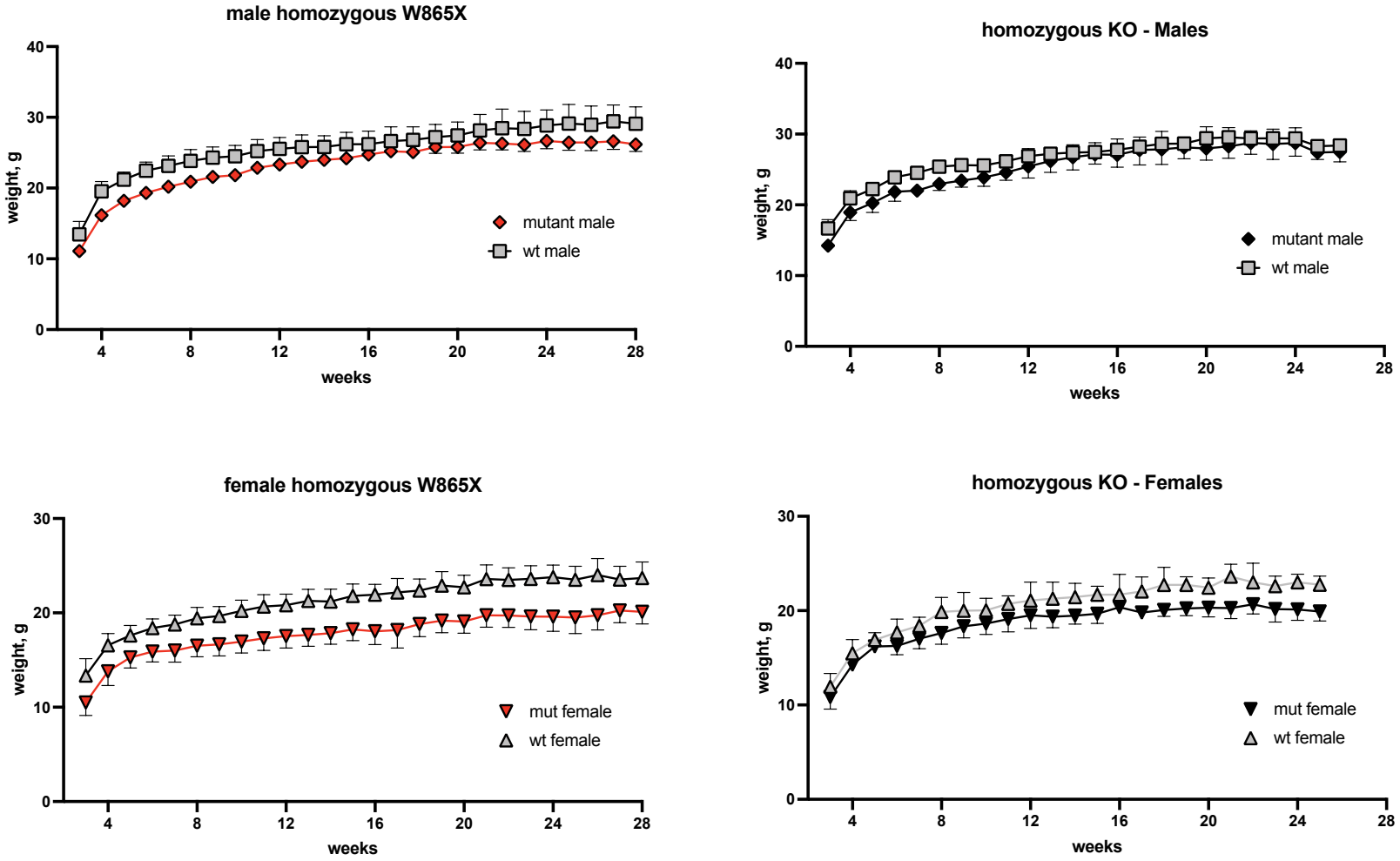

Supplemental Figure 2. Uncropped western image. Full blot of lanes presented in Figure 2B. Middle portion of the blot was removed to eliminate samples not presented in this study.

Supplemental Figure 2

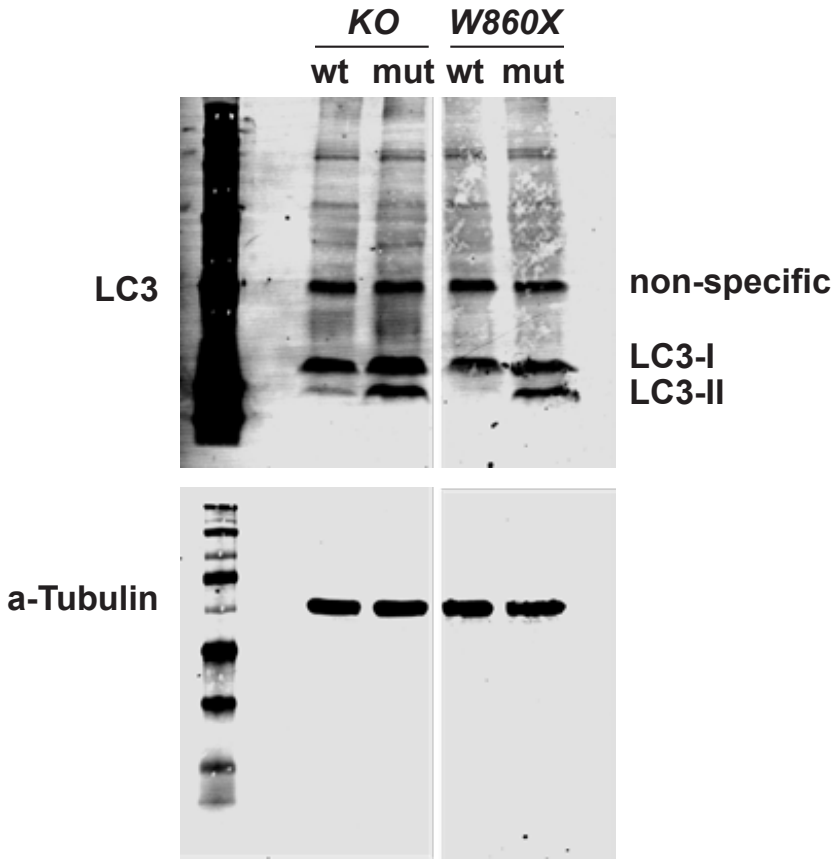

Supplemental Figure 3. Additional gene expression analysis of spinal cord tissues from *W860X* and *KO* homozygous mutant mice compared to wildtype control sibling mice.

Supplemental Figure 3

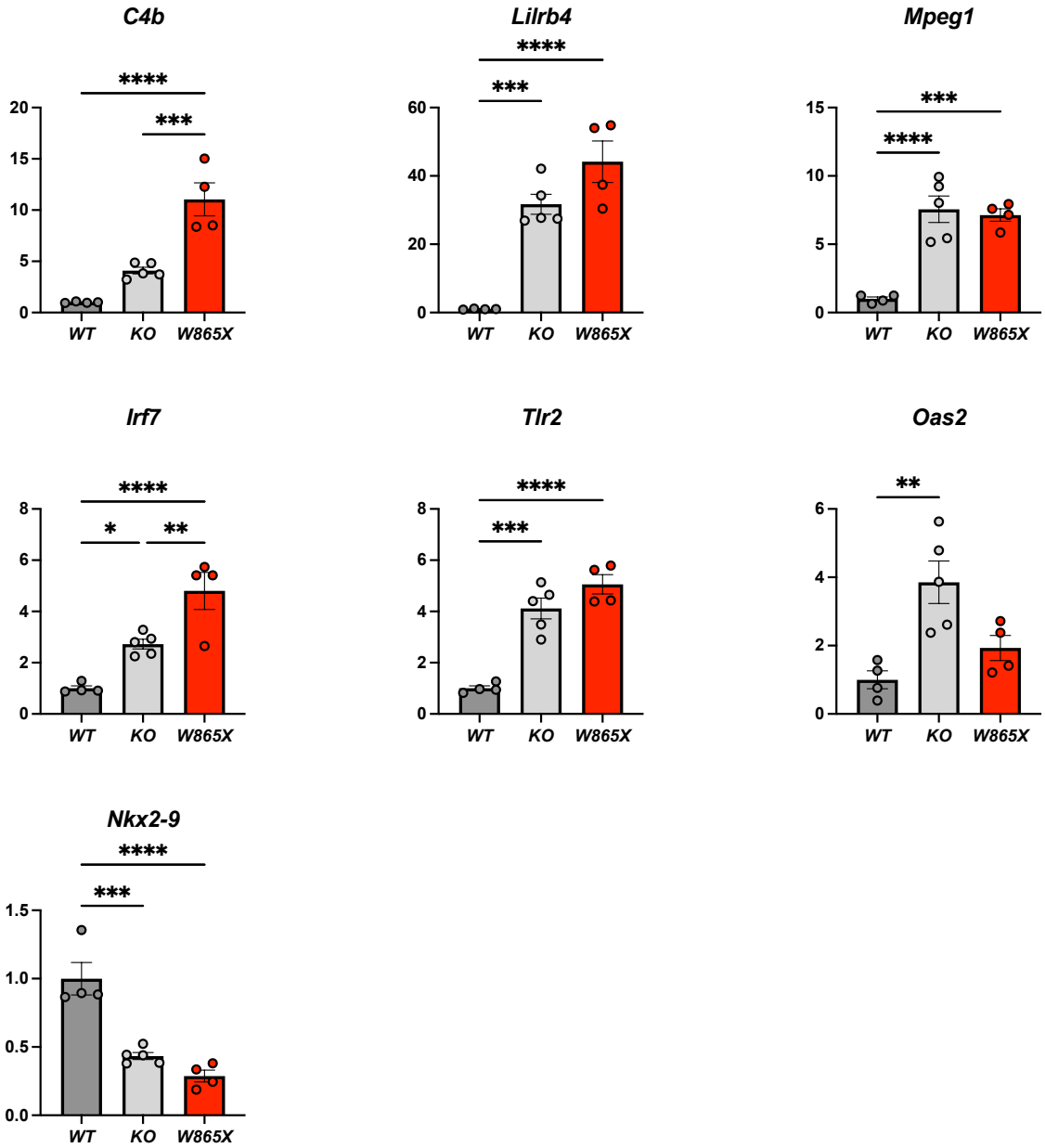

Supplemental Figure 4. Additional gene expression analysis of cerebellum tissues from *W860X* and *KO* homozygous mutant mice compared to wildtype control sibling mice.

Supplemental Figure 4

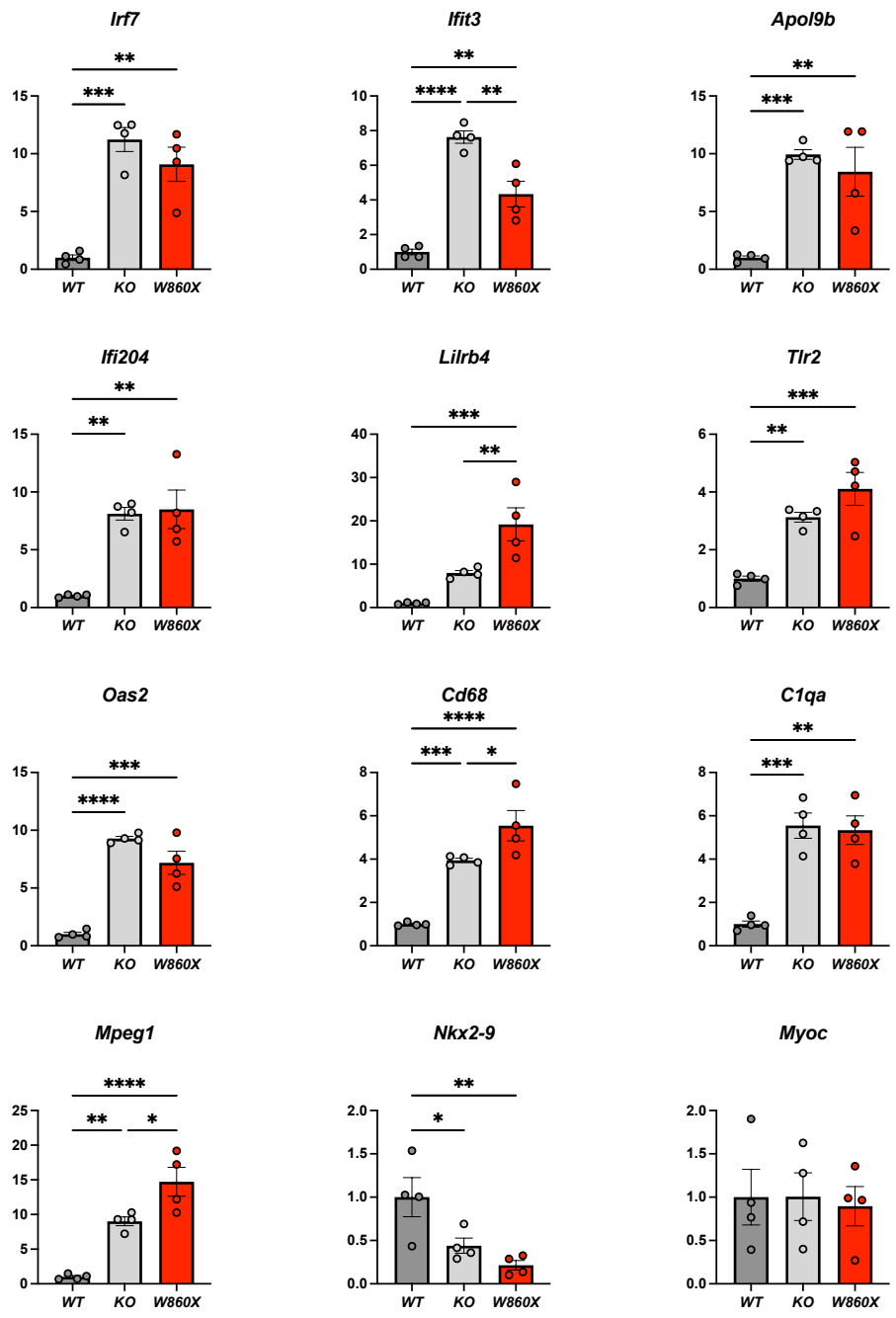

Supplemental Figure 5. Additional gene expression analysis of spinal cord and cerebellum tissues at 2 months and 6 months of age from *W860X* and *KO* homozygous mutant mice compared to wildtype control sibling mice.

Supplemental Figure 5

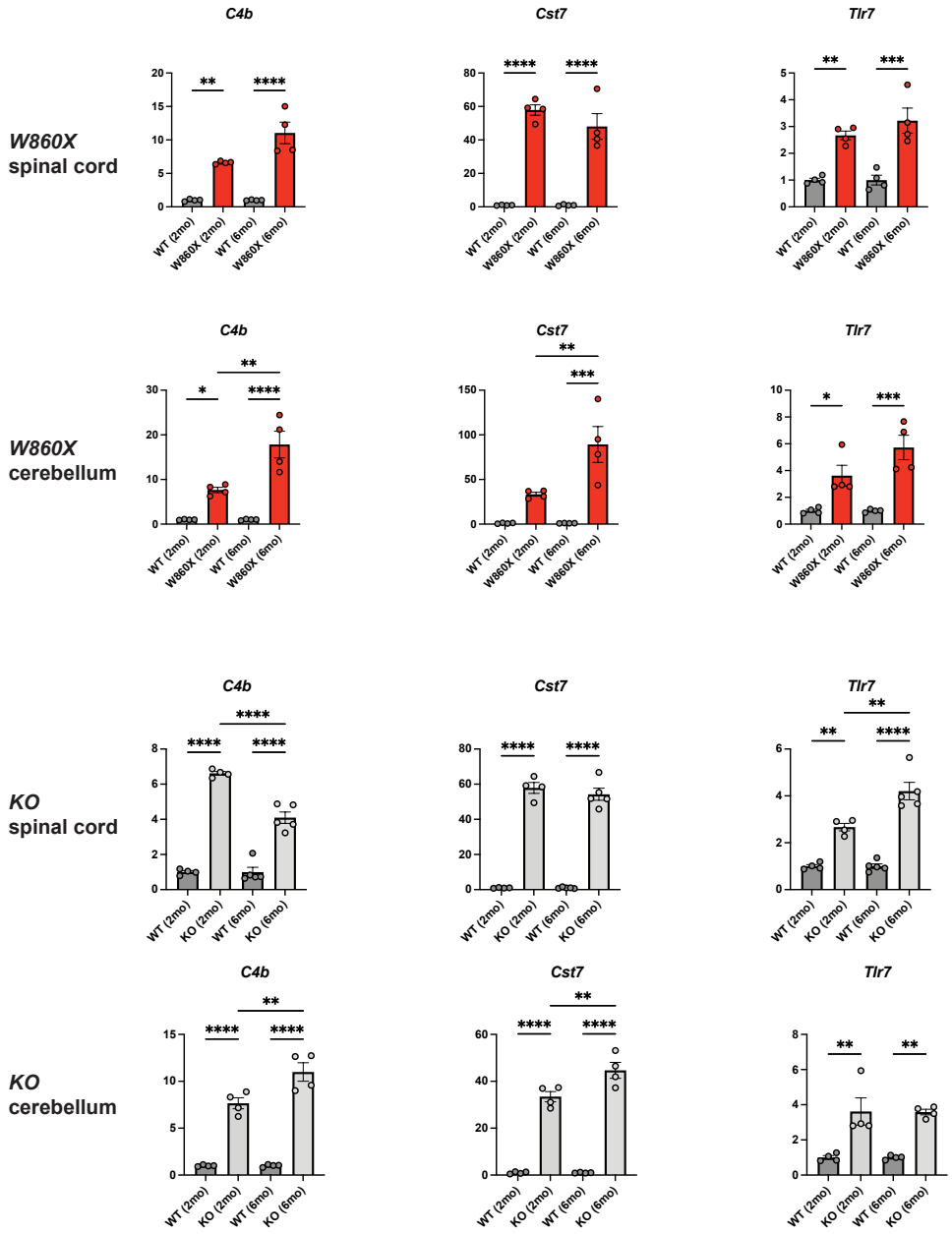

Supplemental Movie 1. Ataxic locomotion associated with *Epg5 W860X* homozygous mutant mice. W860X homozygous mutant male ('Mutant) or wildtype control littermate ('Wildtype') at 7 months of age were monitored in their home cage for capacity to walk and navigate cage. Note ataxic movement in W860X homozygous mutant mouse.

Supplemental video 1 screen capture

Supplemental Table 1. Summary of *Epg5* mutant alleles

Mouse allele	MGI allele nomenclature	mutation	Epg5 exon	crRNA target sequence	Donor DNA sequence	Forward Primer	Reverse Primer	Final allele sequence
KO	em1Vvn	p.R41QfsTer8	2	CGGGCTCTCCTGCTCGCGAC	n/a	AACTCCTCATGCTGAAACCACT	CCTCTCCCCTTTCTTTTAGGTCC	AACTCCTCATGCTGAAACCACTAGCTCTTTTATATCTCCTGCCTTGCTTGTAGGAAAGAAGAAGCATGAAGCCCTTCAGACTTGTGATGCAGGTCCCCTGCCAGAGACCTGTCAGCTTCTGAACTCAAAGGAGATGACCTGAAGTCGTCTGCTGACCCCCAGCTCCACAGTGATGTGTGTGGATGGAATGAAAGTGAGATGTTTGATATACCACTCACCTCCTTGACTATAGGGGATGAAGGTCCCCCGGTACAGGACACAGAGGACCTAAAAGAAAGGGGAGAGG
W860X	em2Vvn	W860X	14	CCCGAATCACAGCTATCTCT	ATAATGTTCTTGTCTTAAATTTAATTATTATTGTTTTCTTTTTAAAAAGGTTTCTTTATACTTGTTTAAAGAACTGCCTTTGTATCTTTGAAGAATTCCGACCTTCTGCCCTAGAGATAGCTGTGATTCGGGACTGGTTATTGAATAATAATCTGACAGCAGTGAAGAACAAGTTGGCCT	CATCTTTTCCAAGGAAATTCTGCAA	AGGCTCCTACTTCTCGGAAATG	CATCTTTTCCAAGGAAATTCTGCAAGAGTTTAATAATGTTCTTGTCTTAAATTTAATTATTATTGTTTTCTTTTTAAAAAGGTTTCTTTATACTTGTTTAAAGAACTGCCTTTGTATCTTTGAAGAATTCCGACCTTCTGCCCTAGCTGTGATTCGGGACTGGTTATTGAATAATAATCTGACAGCAGTGAAGAACAAGTTGGCCTGTGTGATCCTAGAAGGACTGAATTGGGGATTACTGAACAGGTATGCCATTTCCGAGAAGTAGGAGCCT

mouse acces NM_001195633.2

Supplemental Table 2. ThermoFisher TaqMan Gene Expression Assays used in this study.

Gene	Assay ID
C4b	Mm00437890_m1
Cst7	Mm00438351_m1
Gapdh	Mm99999915_g1
Gfap	Mm01253033_m1
Gpnmb	Mm01328587_m1
Irf7	Mm00516788_m1
Itgax	Mm00498701_m1
Lilrb4a	Mm01614371_m1
Epg5	Mm01257763_m1
Mpeg1	Mm01222137_g1
Myoc	Mm00447900_m1
Nkx2-9	Mm00435145_m1
Oas2	Mm00460961_m1
Tlr2	Mm00442346_m1
Tlr7	Mm00446590_m1

Supplemental Table 3. Overlapping differentially expressed genes between spinal cord and cereb

		Spinal cord		Cerebellum		
		Log2 (FC)	padj	Log2 (FC)	padj	
9930111J21R	9930111J21R	1.09323696	6.98E-16	1.33038402	0.00322291	
Abcc3	Abcc3	2.12550858	1.73E-07	1.56327374	0.00217837	
Adgre1	Adgre1	3.08041469	5.13E-165	2.33614275	2.62E-26	
Apobec1	Apobec1	2.43876645	2.34E-63	1.4175323	1.27E-06	
Arhgap25	Arhgap25	1.75621845	7.46E-22	1.32557032	0.00448986	
Arhgap30	Arhgap30	1.56735543	9.94E-58	1.41747037	0.00015443	
Arhgap45	Arhgap45	1.31513497	5.85E-43	1.04870243	1.24E-07	
Aspg	Aspg	2.72973722	3.93E-158	1.70045847	1.19E-20	
Atf3	Atf3	2.70013561	1.17E-30	1.02539951	0.00363607	
B2m	B2m	1.99016329	1.24E-134	2.13836775	1.95E-152	
B430306N03	B430306N03	3.26968387	1.11E-26	4.50528311	6.23E-08	
Blnk	Blnk	1.56527998	1.92E-28	1.66418325	5.93E-05	
Bst2	Bst2	2.32672814	4.18E-50	3.03118447	4.73E-55	
C1qa	C1qa	2.83889106	1.02E-181	2.42318726	5.95E-140	
C1qb	C1qb	2.4770435	3.95E-130	1.98774015	7.96E-73	
C1qc	C1qc	2.48082661	6.62E-158	2.03478932	2.60E-86	
C1ra	C1ra	3.11896874	3.44E-62	1.24464176	0.0079316	
C3	C3	2.97293034	1.85E-226	3.6966202	1.87E-67	
C3ar1	C3ar1	2.77905432	1.79E-99	2.49205263	4.79E-20	
C4b	C4b	3.24945218	0	4.097653	0	
Capn11	Capn11	-1.6181141	1.95E-05	-1.8847395	3.56E-06	*
Casp12	Casp12	2.06220661	3.80E-90	1.10847482	1.82E-07	
Casp4	Casp4	1.12751752	5.53E-07	2.39660891	0.00043959	
Ccl12	Ccl12	3.36680058	1.67E-09	3.76551008	0.00014058	
Ccl3	Ccl3	3.96950057	1.91E-29	3.51187528	2.67E-05	
Ccl5	Ccl5	1.99112676	0.00042323	3.45421804	6.25E-05	
Cd109	Cd109	2.233577	2.89E-81	1.56588797	1.52E-07	
Cd180	Cd180	1.745439	3.00E-19	2.11347131	1.90E-13	
Cd22	Cd22	2.453873	1.62E-05	3.74602405	2.95E-13	
Cd300c2	Cd300c2	2.10913094	4.18E-50	1.98900905	2.17E-08	
Cd300lf	Cd300lf	1.42525364	8.90E-19	2.20563695	0.00023274	
Cd33	Cd33	1.40523312	5.06E-15	1.50917871	5.72E-10	
Cd37	Cd37	1.39699777	7.46E-16	1.3810384	9.34E-08	
Cd4	Cd4	2.36723969	4.51E-05	2.36629778	0.00365418	
Cd44	Cd44	1.62018019	8.61E-54	1.11814697	1.45E-22	
Cd48	Cd48	3.81773186	7.06E-87	2.48453573	3.16E-07	
Cd52	Cd52	3.18278585	9.67E-80	2.23261055	2.65E-07	
Cd53	Cd53	1.64481494	1.52E-51	1.4575883	5.46E-08	
Cd68	Cd68	3.3192545	8.49E-293	2.30429753	9.08E-61	
Cd84	Cd84	2.07652747	3.81E-143	2.55015394	1.13E-22	

Cd86	Cd86	1.29260542	1.09E-10	1.69325869	0.00075391
Cebpd	Cebpd	3.04244063	1.24E-110	1.3648677	1.33E-07
Cp	Cp	2.3877424	4.68E-209	1.01235372	1.34E-21
Csf2rb	Csf2rb	2.23505878	1.63E-34	2.00183887	9.18E-06
Csf3r	Csf3r	1.77824849	1.91E-47	1.78261377	8.94E-18
Cst7	Cst7	7.08358303	1.27E-73	5.59410643	2.30E-13
Ctsh	Ctsh	1.66905581	2.22E-18	1.04331553	1.96E-12
Ctss	Ctss	2.04824464	1.34E-99	2.03825339	1.25E-99
Cxcl10	Cxcl10	3.20387296	6.57E-07	4.49244054	3.57E-26
Cxcl16	Cxcl16	2.4554051	7.76E-27	1.5013931	1.33E-07
Cxcl5	Cxcl5	1.95920013	2.92E-15	2.81624929	3.48E-06
Cxcr4	Cxcr4	1.7517299	1.19E-42	1.71181145	1.42E-06
Cyba	Cyba	2.55570313	3.96E-93	1.21737819	1.63E-06
Cybb	Cybb	3.31367843	1.11E-185	2.58867483	9.72E-15
Cybrd1	Cybrd1	1.07973224	2.89E-16	1.63721629	8.61E-13
Cyp1b1	Cyp1b1	1.3389824	3.25E-27	1.05310163	9.07E-05
Cyth4	Cyth4	1.17195832	1.11E-23	1.32300354	1.78E-10
Ddx60	Ddx60	2.130275	1.54E-28	3.99673794	9.12E-49
Dock2	Dock2	1.89784946	3.35E-11	1.57202733	2.57E-07
Dram1	Dram1	1.06683997	0.00036719	1.35714395	0.0081225
Elf4	Elf4	1.93386756	6.40E-19	1.41327999	6.53E-05
Emp3	Emp3	1.79141591	0.00077939	1.22367421	0.00075711
Endou	Endou	1.87109118	1.98E-31	1.92810235	6.80E-08
Epsti1	Epsti1	1.95196933	1.74E-12	2.81745101	4.02E-06
Fcer1g	Fcer1g	2.57228129	9.12E-20	2.14359677	4.88E-23
Fcgr2b	Fcgr2b	3.38787	2.57E-210	2.74587265	1.89E-34
Fcgr3	Fcgr3	1.656828	3.43E-53	1.45545798	1.96E-13
Fcrls	Fcrls	2.9554464	8.90E-256	2.21805027	1.39E-42
Fermt3	Fermt3	1.41069548	2.83E-24	1.28014374	4.38E-06
Fgr	Fgr	3.2053797	3.17E-53	2.65315916	0.00585116
Flnc	Flnc	1.56141239	1.81E-99	1.24577877	2.69E-19
Ftl1	Ftl1	1.8844304	9.92E-185	1.01330848	5.80E-75
Fyb	Fyb	2.17330256	1.02E-63	1.82447571	4.27E-12
Gbp10	Gbp10	3.96787969	3.50E-05	4.44224147	3.47E-30
Gbp2	Gbp2	2.03551463	2.58E-77	1.98818105	8.70E-40
Gbp3	Gbp3	1.59621172	1.35E-41	2.68173003	2.94E-74
Gbp5	Gbp5	1.60396385	1.75E-31	1.64147129	1.04E-15
Gbp6	Gbp6	2.53213722	6.28E-119	3.88841536	2.62E-89
Gbp7	Gbp7	1.13764387	1.23E-20	2.15340475	4.09E-39
Gbp9	Gbp9	1.2293972	2.92E-13	1.75609935	3.68E-30
Gfap	Gfap	1.859965	2.41E-187	2.42280036	0
Gm4951	Gm4951	1.62456055	3.88E-12	4.42584264	2.69E-20
Gna15	Gna15	1.11235084	3.95E-05	1.17244283	0.00265629

Gpnmb	Gpnmb	6.96937547	0	3.11687788	2.36E-107
Gpsm3	Gpsm3	1.31165269	4.37E-06	1.09670299	0.00227162
Gpx3	Gpx3	1.751674	1.79E-44	2.11788307	1.07E-05
Gsdmd	Gsdmd	1.08427717	3.99E-10	1.07954077	1.92E-05
H2-K1	H2-K1	1.53826538	4.01E-43	1.87352754	4.21E-12
H2-Q4	H2-Q4	1.17785503	3.74E-27	2.23186312	1.13E-08
H2-Q6	H2-Q6	1.35268617	6.68E-41	3.32350483	1.51E-05
H2-Q7	H2-Q7	1.43095142	1.40E-23	2.65803239	7.67E-13
H2-T23	H2-T23	1.17789121	5.25E-17	1.9377008	1.70E-51
Hacd4	Hacd4	2.48283111	3.56E-78	1.05527605	0.00017758
Havcr2	Havcr2	1.43021189	3.17E-23	1.55293502	0.00011274
Hck	Hck	1.63157853	9.90E-30	1.89681402	6.73E-06
Hcls1	Hcls1	1.72310648	8.01E-20	1.21891204	6.07E-10
Herc6	Herc6	1.17841776	6.75E-18	2.04998062	2.02E-21
Hmox1	Hmox1	2.0949206	4.74E-101	1.15696662	9.42E-07
Hpgds	Hpgds	1.10793338	1.30E-32	1.35408527	2.63E-10
Hpse	Hpse	4.04279887	2.57E-119	3.89997715	2.63E-17
Hvcn1	Hvcn1	2.87627013	9.57E-97	2.2310342	5.67E-16
Icam1	Icam1	2.33021974	4.98E-100	1.53898644	1.62E-11
Ifi204	Ifi204	1.74784008	1.44E-16	4.26484537	1.32E-25
Ifi206	Ifi206	3.76255694	4.23E-06	6.37423246	5.88E-16
Ifi207	Ifi207	4.75417028	1.07E-32	4.31043902	6.63E-25
Ifi209	Ifi209	2.15622861	1.10E-12	3.83016174	1.08E-07
Ifi211	Ifi211	3.25123308	3.75E-11	5.54861776	1.40E-05
Ifi213	Ifi213	1.20489433	1.03E-06	4.60156466	1.35E-24
Ifi27l2a	Ifi27l2a	3.09415307	8.32E-33	4.5272449	4.88E-12
Ifi35	Ifi35	1.01853263	1.28E-11	1.78594362	2.75E-10
Ifi44	Ifi44	2.1088134	2.13E-20	3.43396532	1.41E-33
Ifi47	Ifi47	1.71500301	7.11E-11	2.71436936	1.40E-10
Ifih1	Ifih1	1.15167678	7.44E-15	1.98325284	4.53E-48
Ifit1	Ifit1	1.80210266	9.03E-36	4.33450463	7.10E-221
Ifit3	Ifit3	1.58082475	3.87E-12	3.43150581	3.34E-60
Ifit3b	Ifit3b	1.52220083	4.06E-38	3.29314397	7.43E-147
Ifitm3	Ifitm3	1.82946232	4.97E-70	2.43416081	6.56E-56
Igsf6	Igsf6	2.52037471	1.25E-32	2.07354986	0.00037128
Igtp	Igtp	1.00030597	2.69E-15	2.89889032	1.23E-62
Iigp1	Iigp1	1.24035482	6.42E-13	2.34398713	3.97E-24
Ikzf1	Ikzf1	1.3934617	8.33E-18	1.29298109	5.95E-06
Inpp5d	Inpp5d	1.27190344	6.54E-29	1.24737539	2.20E-10
Irf5	Irf5	1.21467096	1.59E-09	1.45034757	3.46E-06
Irf7	Irf7	1.79885208	3.39E-14	4.27563941	1.19E-189
Irf8	Irf8	1.75961838	1.86E-43	1.469239	5.83E-10
Irf9	Irf9	1.41117651	1.74E-42	2.19934043	1.40E-127

Irgm1	Irgm1	1.29359346	1.36E-42	2.84748724	7.70E-135	
Irgm2	Irgm2	1.40746868	7.76E-31	2.35813783	4.33E-12	
Isg15	Isg15	1.97567196	5.42E-11	3.53013719	2.10E-37	
Itgam	Itgam	1.39487586	1.08E-50	1.4785927	0.00015012	
Itgax	Itgax	4.86246051	1.09E-90	2.94781726	2.42E-07	
Itgb2	Itgb2	2.65340641	2.09E-134	2.12792947	6.59E-25	
Kcns1	Kcns1	1.82837515	3.09E-56	1.193473	5.00E-06	
Laptm5	Laptm5	1.71192945	2.20E-115	1.55676397	3.90E-41	
Lcn2	Lcn2	8.23824511	6.01E-175	6.98157203	9.14E-17	
Lcp2	Lcp2	1.15918121	8.83E-08	1.57088278	1.98E-05	
Lgals3	Lgals3	3.21109024	6.56E-05	2.6015204	9.07E-32	
Lgals3bp	Lgals3bp	2.58888466	4.35E-115	3.20785225	7.22E-23	
Lgals9	Lgals9	1.23594525	4.94E-12	2.31785955	2.22E-61	
Lilrb4a	Lilrb4a	6.11679115	1.24E-207	3.64229431	2.99E-10	
Ly86	Ly86	1.31532624	6.32E-28	1.28221394	1.69E-07	
Ly9	Ly9	6.23861607	1.88E-116	4.55341404	2.71E-23	
Lyz2	Lyz2	5.91046957	0	2.76446151	6.99E-121	
Mafb	Mafb	1.22837804	1.23E-34	1.19402998	5.03E-11	
Met	Met	1.51339207	1.19E-21	1.81739235	0.00015166	
Mmp19	Mmp19	2.39631242	9.66E-56	1.14488893	0.00961152	
Mmrn2	Mmrn2	1.07996509	1.31E-08	1.16303462	8.17E-12	
Mndal	Mndal	1.18258563	6.07E-07	2.01059136	2.11E-14	
Mpeg1	Mpeg1	3.24940321	1.39E-278	2.6585749	2.95E-163	
Ms4a6b	Ms4a6b	2.29815961	7.68E-19	2.64518093	1.96E-06	
Ms4a6c	Ms4a6c	4.30058984	6.35E-89	2.67681065	9.55E-06	
Ms4a6d	Ms4a6d	3.04188719	9.87E-61	2.78686839	4.98E-08	
Ms4a7	Ms4a7	3.53125441	9.59E-82	2.87197894	0.00019914	
Myo1f	Myo1f	2.57091034	2.31E-80	1.86017073	3.91E-15	
Naip2	Naip2	1.72924888	4.53E-44	2.0926213	1.45E-06	
Naip5	Naip5	1.63477516	6.45E-25	1.44817403	0.00402905	
Ncf1	Ncf1	1.80737296	1.29E-63	1.56973261	7.66E-11	
Nckap1l	Nckap1l	1.50529251	3.41E-59	1.39158974	4.56E-09	
Nfam1	Nfam1	1.580226	1.67E-31	1.24620575	0.00304052	
Nkx2-9	Nkx2-9	-1.7853189	6.56E-24	-1.5363872	0.0012498	*
Nlrc5	Nlrc5	2.25657049	3.13E-28	3.02177144	1.84E-08	
Oas1a	Oas1a	2.55551833	8.45E-23	3.89118159	2.50E-32	
Oas1g	Oas1g	3.42955597	1.06E-18	4.80820977	1.60E-17	
Oas2	Oas2	3.18867506	2.22E-26	4.02275279	2.65E-20	
Oasl1	Oasl1	1.33293957	0.00199826	3.64436117	3.60E-23	
Oasl2	Oasl2	1.59728013	8.59E-15	4.5741957	0	
Osgin1	Osgin1	3.00950338	2.73E-18	1.597678	0.00047451	
Osmr	Osmr	2.60423198	4.54E-106	1.29034216	8.51E-14	
P2ry6	P2ry6	1.60154361	3.59E-15	1.28417266	0.00361603	

Parp10	Parp10	1.15464847	1.49E-13	1.75256971	3.62E-14
Parp14	Parp14	1.62123279	6.98E-33	2.7252473	2.93E-94
Phf11b	Phf11b	1.43054	0.00062	3.52445404	2.60E-06
Phf11d	Phf11d	1.301265	4.97E-07	3.07515079	8.32E-12
Pik3ap1	Pik3ap1	1.75375416	4.19E-62	1.61840688	2.94E-10
Pik3cg	Pik3cg	1.41647866	5.57E-35	1.5509373	1.51E-07
Pik3r5	Pik3r5	1.34886588	7.37E-24	1.47278377	0.00056886
Pirb	Pirb	3.47346512	1.90E-77	3.17641247	7.93E-11
Pla2g5	Pla2g5	1.0454165	2.22E-09	1.5300915	1.75E-08
Plau	Plau	2.44026133	1.07E-53	1.38022124	0.00867992
Plaur	Plaur	2.46744804	1.08E-17	1.31527775	0.00258336
Plcg2	Plcg2	1.56947193	2.78E-72	1.08154153	2.09E-06
Pld4	Pld4	1.2023639	4.28E-15	1.21704964	1.15E-07
Plscr2	Plscr2	1.34768233	4.24E-22	1.09168062	1.70E-05
Psmb8	Psmb8	2.21546109	2.41E-09	2.12590838	1.46E-21
Psmb9	Psmb9	1.37956227	7.48E-09	2.09133326	3.24E-10
Ptafr	Ptafr	1.86952626	8.90E-28	2.52990537	3.34E-07
Ptgs2	Ptgs2	1.77551623	4.95E-14	2.09768419	0.00051199
Ptpn6	Ptpn6	1.90240483	4.78E-16	1.89198975	1.44E-18
Ptprc	Ptprc	1.66898916	5.19E-67	1.98218167	3.05E-12
Pycard	Pycard	1.67769381	9.20E-25	1.24016306	0.00014135
Qprt	Qprt	1.07912428	0.0003234	1.06267953	0.0026013
Rac2	Rac2	1.25024663	7.28E-12	1.39076245	0.00047451
Rasal3	Rasal3	1.38812073	4.09E-11	1.15441901	0.00133359
Rnf213	Rnf213	1.02936303	4.53E-44	2.92297347	1.60E-269
Rsad2	Rsad2	2.39190388	8.86E-67	4.05477845	1.16E-111
Rtp4	Rtp4	1.33458926	6.19E-22	4.02740414	1.78E-81
S1pr3	S1pr3	2.15344914	4.62E-95	1.06766959	2.29E-07
Samsn1	Samsn1	1.888985	6.79E-22	1.54356173	0.00908748
Sash3	Sash3	1.6070489	2.65E-16	1.2284922	0.00995937
Sctr	Sctr	2.03428616	2.22E-18	2.18036048	0.00979115
Serpina3n	Serpina3n	4.31870614	0	2.69367338	4.53E-62
Siglec1	Siglec1	4.15375252	1.88E-116	3.07308979	4.05E-20
Slamf9	Slamf9	2.381156	6.04E-33	1.56869667	0.00839036
Slc11a1	Slc11a1	3.338065	6.41E-25	2.25945412	1.75E-20
Slc15a3	Slc15a3	2.202387	2.80E-39	1.03871766	0.00248646
Slc43a3	Slc43a3	3.391145	1.20E-78	2.20339326	4.14E-11
Slfn2	Slfn2	2.44927594	2.69E-37	2.30845658	4.57E-07
Slfn5	Slfn5	1.22815019	4.24E-23	1.34205719	5.41E-39
Slfn8	Slfn8	1.81435195	1.09E-19	3.45993299	1.17E-31
Sp100	Sp100	1.21268615	4.56E-17	1.69431912	1.39E-36
Sp110	Sp110	1.26909943	4.11E-13	1.89702199	3.59E-10
Sp140	Sp140	2.31027467	1.84E-10	1.85005001	0.00063355

Spi1	Spi1	1.64679025	1.61E-07	1.30648573	3.36E-06
Stab1	Stab1	1.412411	1.78E-13	1.13929771	6.53E-19
Syk	Syk	1.70671096	3.47E-42	1.61450849	7.14E-10
Tap1	Tap1	1.04311893	2.30E-09	1.90580866	7.45E-23
Tent5c	Tent5c	1.90704566	3.33E-61	1.09685559	0.00014035
Tgtp1	Tgtp1	1.14313856	0.00238102	2.27638666	9.39E-07
Themis2	Themis2	1.947071	2.96E-25	1.88186106	1.23E-06
Timp1	Timp1	6.72298999	9.38E-96	2.13374215	0.00279707
Tlr13	Tlr13	2.32753293	2.72E-91	1.91674908	1.42E-06
Tlr2	Tlr2	2.58309712	4.29E-120	2.25703879	2.65E-14
Tlr7	Tlr7	2.23676878	2.73E-31	2.12004101	2.58E-11
Tmem106a	Tmem106a	1.84723862	2.65E-15	1.83369932	0.00023074
Tmem140	Tmem140	1.09860098	4.14E-08	1.40385403	9.85E-06
Tmem176a	Tmem176a	2.23273212	5.05E-27	1.29958885	1.91E-11
Tnfrsf1b	Tnfrsf1b	1.36348076	0.00263848	1.70122722	1.29E-11
Trem2	Trem2	2.58713712	8.40E-195	2.18780217	2.09E-44
Treml2	Treml2	2.42613098	2.81E-22	3.41506429	6.92E-07
Trim12c	Trim12c	1.058529	3.19E-17	1.71640508	7.22E-15
Trim30a	Trim30a	1.81813707	9.97E-35	3.16077017	2.39E-72
Tubb6	Tubb6	1.25448578	8.35E-16	1.140325	0.00350475
Tyrobp	Tyrobp	2.75002265	8.32E-96	1.84897965	8.43E-34
Uba7	Uba7	1.08654111	9.84E-19	1.98942687	6.54E-31
Unc93b1	Unc93b1	1.28069625	1.58E-28	1.29184662	1.94E-21
Usp18	Usp18	2.26246116	9.81E-20	4.36206577	1.25E-99
Vav1	Vav1	1.78895641	8.18E-26	1.2688305	6.99E-05
Wdfy4	Wdfy4	1.22520348	4.49E-06	1.53619436	0.00016596
Xdh	Xdh	1.71104141	4.05E-39	1.21164822	3.28E-25
Zbp1	Zbp1	4.02148415	1.45E-19	4.63812852	5.92E-34
Zc3hav1	Zc3hav1	1.00055704	1.01E-36	2.02025225	3.05E-75